

Efficient 3D Reconstruction, Streaming and Visualization of Static and Dynamic Scene Parts for Multi-client Live-telepresence in Large-scale Environments

Leif Van Holland^a, Patrick Stotko^a, Stefan Krumpen^a, Reinhard Klein^a, Michael Weinmann^{a,b,*}

^aUniversity of Bonn, Regina-Pacis-Weg 3, Bonn, 53113, Germany

^bDelft University of Technology, Mekelweg 5, Delft, 2628 CD, Netherlands

Abstract

Despite the impressive progress of telepresence systems for room-scale scenes with static and dynamic scene entities, expanding their capabilities to scenarios with larger dynamic environments beyond a fixed size of a few square-meters remains challenging.

In this paper, we aim at sharing 3D live-telepresence experiences in large-scale environments beyond room scale with both static and dynamic scene entities at practical bandwidth requirements only based on light-weight scene capture with a single moving consumer-grade RGB-D camera. To this end, we present a system which is built upon a novel hybrid volumetric scene representation in terms of the combination of a voxel-based scene representation for the static contents, that not only stores the reconstructed surface geometry but also contains information about the object semantics as well as their accumulated dynamic movement over time, and a point-cloud-based representation for dynamic scene parts, where the respective separation from static parts is achieved based on semantic and instance information extracted for the input frames. With an independent yet simultaneous streaming of both static and dynamic content, where we seamlessly integrate potentially moving but currently static scene entities in the static model until they are becoming dynamic again, as well as the fusion of static and dynamic data at the remote client, our system is able to achieve VR-based live-telepresence at close to real-time rates. Our evaluation demonstrates the potential of our novel approach in terms of visual quality, performance, and ablation studies regarding involved design choices.

Keywords: Telepresence, Virtual Reality, Scene Reconstruction, Streaming, Dynamic Scenes, 3D Computer Vision

1. Introduction

Sharing immersive, full 3D experiences with remote users, while allowing them to explore the respectively shared places or environments individually and independently from the sensor configuration, represents a core element of *metaverse* technology. Beyond pure 2D images or 2D videos, 3D telepresence is defined as the impression of individually *being there* in an environment that may differ from the user's actual physical environment [1–5]. This offers new opportunities for diverse applications including remote collaboration, entertainment, advertisement, teaching, hazard site exploration, rehabilitation as well as for joining virtual sports events, work meetings, remote inspection, monitoring and maintenance, consulting applications or simply enjoying social gatherings. In turn, the possibilities for virtually bringing people or experts together from all over the world in a digital twin of a location as well as the live-virtualization of such environments and events may reduce the effort regarding on-site traveling for many people, which not only helps to reduce our CO_2 footprint and increase the efficiency of various processes due to time savings, but also facilitates economically less well-situated or handicapped people to access such environments or events.

The creation of an immersive telepresence experience relies on various factors. Respective core features are visually con-

vincing depictions of a scenario as well as the subjective experience, vividness and interactivity in terms of operating in the scene [6, 7]. Therefore, the involved aspects include display parameters (e.g., resolution, frame rate, contrast, etc.), the presentation of the underlying data, its consistency, low-latency control to avoid motion sickness, the degree of awareness and the suitability of controller devices [1–7]. Furthermore, experiencing 3D depth cues like stereopsis, motion parallax, and natural scale also contribute to the perceived level of immersion and copresence [8, 9].

However, such immersive 3D scene exploration experience becomes particularly challenging for telepresence in live-captured environments due to the additional requirement of accurately reconstructing the digital twin of the underlying scene on the fly as well as its efficient streaming and visualization to remote users under the constraints imposed by available network bandwidth and client-side compute hardware. Among many approaches, impressive immersive AR/VR-based live-3D-telepresence experiences have only been achieved based on advanced RGB-D acquisition for dynamic scenes on the scale of rooms, i.e. areas of only a few square-meters, using special expensive static capture setups [10–25] and display technology [25], as well as for static scenes beyond that scale based on low-cost and light-weight incremental scene capture with a moving depth camera [26–30]. For the latter category, bandwidth requirements have been reduced from hundreds of MBit/s for a single user [26] to around 15MBit/s for group-scale shar-

*Corresponding author



Figure 1: Visualization of the key components of our proposed pipeline. The color image is blended with class and instance information, and shown along with the optical flow with respect to the previous frame (first image). This information is integrated to produce a mask that segments the frame into static and dynamic regions (second image). Together with an accumulated 3D motion estimate (third image), the scene is streamed to one or multiple remote clients for immersive exploration in VR (fourth image).

ing of telepresence in live-captured environments while also handling network interruptions [27, 28, 30], thereby even allowing live-teleoperation of robots [29]. However, expanding the capabilities and, thereby overcoming the aforementioned limitations in large dynamic environments for many users with low-cost setups still remains an open challenge.

In this paper, we aim at sharing 3D live-telepresence experiences in large-scale environments beyond room scale with *both static and dynamic scene entities* at practical bandwidth requirements and based on light-weight scene capture with a single moving consumer-grade RGB-D camera. For this purpose, we propose a respective system that relies on efficient 3D reconstruction, streaming and immersive visualization for dynamic large-scale scenes.

In particular, the key contributions of our work are:

- For the sake of efficiency, our system leverages a hybrid volumetric scene representation, where we use optical flow and instance information extracted from the input frames to detect static and dynamic scene entities, thereby allowing the combination of a classic implicit surface geometry representation enriched with the object semantics as well as their accumulated dynamic motion over time, with a point-cloud-based representation of dynamic parts.
- We achieve efficient data streaming to remote users by the separate yet simultaneous streaming of both static and dynamics scene information, where we seamlessly integrate potentially moving but currently static scene entities in the static model until they are becoming dynamic again. Additionally, the fusion of static and dynamic data at the remote client allows VR-based visualization of the scene at close to real-time rates.
- We demonstrate the potential of our approach in the scope of several experiments and provide an ablation study for respective design choices.

Furthermore, while not being among the main contributions of our work, our approach also inherits the robustness of previous techniques to network interruptions for the reconstruction of the static scene parts as well as the scalability to group-scale telepresence [27–29]. An overview of our proposed system is depicted in Figure 1.

2. Related Work

Telepresence Systems. Despite almost two decades of progress, the development of systems that allow immersive telepresence experiences remains challenging due to the prerequisite of simultaneously achieving high-fidelity real-time 3D scene reconstruction, the efficient streaming and management of the reconstructed models and the high-quality visualization based on AR and VR equipment. Early approaches were limited by the capabilities of the available hardware [31–36] or inaccurate silhouette-based reconstruction techniques [37, 38]. Depth-based 3D scanning led to improved reconstruction quality and allowed telepresence at the scale of rooms [13, 39–43], however, remaining artifacts induced by the high sensor noise and temporal inconsistency in the reconstruction process still impacted the visual experience. More recently, advances in 3D scene capture, streaming and visualization technology led to impressive immersive AR/VR-based live 3D telepresence experiences. Live-telepresence for small-scale scenarios of a few square-meters has been achieved based on light-weight capture setups for teleconferencing [44–49] and other collaborative scenarios [50–55] as well as based on expensive multi-camera static and pre-calibrated capture setups [10–25]. Furthermore, live-telepresence for scenarios beyond a few square-meters has been achieved based on low-cost and light-weight incremental scene capture with a moving depth camera [26–30, 56, 57], allowing remote users to immersively explore a live-captured environment independent from the sensor configurations. Regarding the latter approaches, impractical bandwidth requirements of up to 175 MBit/s for immersive scene exploration by a single user [26] have been overcome by more recent approaches that allow group-scale sharing of telepresence experiences in live-captured environments while also handling network interruptions [27–30] as well as live-teleoperation of robots [29]. Furthermore, mechanisms for annotation, distance measurement [29] and efficient collaborative VR-based 3D labeling were added [58]. However, practical sharing of live-captured 3D experiences in dynamic large-scale environments for many users with low-cost setup still remains an open challenge. The same applies for immersive robot teleoperation where approaches focused on small-scale scenarios with dynamics [59–65] and large-scale, static scenarios [29].

In contrast to the aforementioned approaches, we propose a live-telepresence system for large-scale environments while also taking scene dynamics into account.

3D Reconstruction and SLAM Techniques. Current state-of-the-art telepresence systems rely on depth-based simultaneous localization and mapping (SLAM) techniques. Examples are the use of depth-sensor-based 3D scene capture based on surfels [66] or extensions of KinectFusion [67, 68] in terms of voxel block hashing techniques [69–73] for incremental scene capture for large-scale telepresence applications [26–30]. To avoid the need for depth sensors, more recent SLAM approaches for incremental scene capture - that might be applicable in respective telepresence applications - leveraged principles of deep learning [74–80]. Further approaches investigated 3D reconstruction from multiple synchronized cameras [81–85].

Recently, neural scene representation and rendering techniques [86, 87] have led to significant improvements in reconstruction quality for small-scale objects or scenes. The underlying idea originates from novel view synthesis and consists of training a neural network to represent a scene with its weights, so that respectively synthesized views match the input photographs. In particular, this includes implicit scene representations based on Neural Radiance Fields (NeRFs) [88] and respective extensions towards speeding up model training [89–95] with training times of seconds, the adaptation to unconstrained image collections [96, 97], deformable scenes [98–108] and video inputs [109–114], the refinement or complete estimation of camera pose parameters for the input images [115–122], combining NeRFs with semantics regarding objects in the scene [123–125], incorporating depth cues [92, 126–129] to guide the training and allow handling textureless regions, handling large-scale scenarios [130, 131], and streamable representations [132]. However, despite promising results, further improvements regarding efficiency are required for the joint camera pose estimation and neural scene reconstruction [118, 119, 133–135] as required in a SLAM setting to achieve beyond the reported 12 FPS on a high-end GPU [134] using small input resolutions while also reducing the time required to reach acceptable reconstruction quality, especially in dynamic scenarios.

Particularly addressing dynamic environments, various approaches focused on filtering dynamic objects and only reconstructing the static background [136–142] or additionally reconstructing the dynamics based on rigid object tracking and reconstruction [143–148] and non-rigid object tracking and reconstruction [149–154, 154–161]. Taking inspiration of the non-rigid scene reconstruction approaches in terms of separating static and dynamic scene parts, the 3D reconstruction approach involved in our live-telepresence system is particularly designed for capturing large-scale environments (i.e., beyond scenarios limited to a small area of a few square-meters) with both static and dynamic entities based on a single moved RGB-D camera. Our hybrid volumetric scene representation leverages semantic and instance information to detect dynamic scene entities and combines a voxel-based scene representation for the static parts, where we also accumulate information on whether and how significant objects have been moved, with a point-cloud-based representation of dynamic parts. A major contribution of our work is the separate but simultaneous

streaming of both static and dynamics scene information and its VR-based visualization at close to real-time rates.

3. Methodology

As shown in Figure 2, our live-telepresence system for large-scale environments with scene dynamics at practical bandwidth requirements takes a continuous stream of RGB-D images $(I_1, D_1), (I_2, D_2), \dots$ from a moving depth camera as input, where $I_k(u) \in \mathbb{R}^3$ represents the red, green and blue color values of frame k , and $D_k(u) \in \mathbb{R}$ the corresponding raw depth measurement at pixel $u \in \mathcal{U} \subset \mathbb{N}^2$, with \mathcal{U} being the image domain. The main challenge consists in an efficient processing of these measurements, their efficient integration into a consistent model and the efficient streaming the latter over the network at practical bandwidth requirements to remote clients, where it has to be visualized at adequate visual quality and at tolerable overall latency. For this purpose, we use a hybrid scene representation that separately handles static and dynamic scene parts, thereby allowing the combination of efficient large-scale 3D scene mapping techniques, that face problems with dynamic regions, with efficient point-based reconstruction for the dynamic parts. In more detail, we segment the frames of the input stream into static and dynamic regions by determining score maps S_k , where $S_k(u) \in \mathbb{R}$ describes the amount of dynamicity in frame k at pixel u . This separation allows us to efficiently reconstruct, stream and immersively visualize static regions using existing state-of-the-art large-scale telepresence techniques [27, 28] while simultaneously reconstructing, streaming and visualizing dynamic scene parts based on a point-based representation in terms of a partial RGB-D image and its corresponding estimated camera pose, thereby limiting the amount of data to be transferred and reducing the processing time. After streaming the hybrid scene representation to remote users, its static and dynamic parts are joined in a combined 3D visualization. In the following subsections, we provide more details on the different steps of our pipeline.

3.1. Segmentation into Static and Dynamic Regions

For the sake of efficiency, we segment the RGB-D frames of the input stream into static and dynamic regions, which will later allow the efficient treatment of the different types of scene parts. For this purpose, we compute score maps S_k , where $S_k(u) \in \mathbb{R}$ describes the amount of dynamicity in frame k at pixel u . In the following, we will assume that these scores are normalized in the sense that a pixel is deemed static if $S_k(u) \leq 1$, and dynamic if $S_k(u) > \tau$, where $\tau \geq 1$ is a threshold that allows for a region of uncertainty between the static and dynamic labels.

Instance Segmentation. To compute the dynamicity score S_k of frame k , we first detect objects in I_k using instance segmentation [162], which yields both a class label and an instance ID for each pixel in the image, i.e. $(L_k, \iota_k) = f_{\text{seg}}(I_k)$ of I_k , where $L_k(u) \in \mathbb{N}$ is the predicted class label and $\iota_k(u) \in \mathbb{N}$ is the instance ID at pixel u . The raw output of the segmentation network may consist of multiple, potentially overlapping region

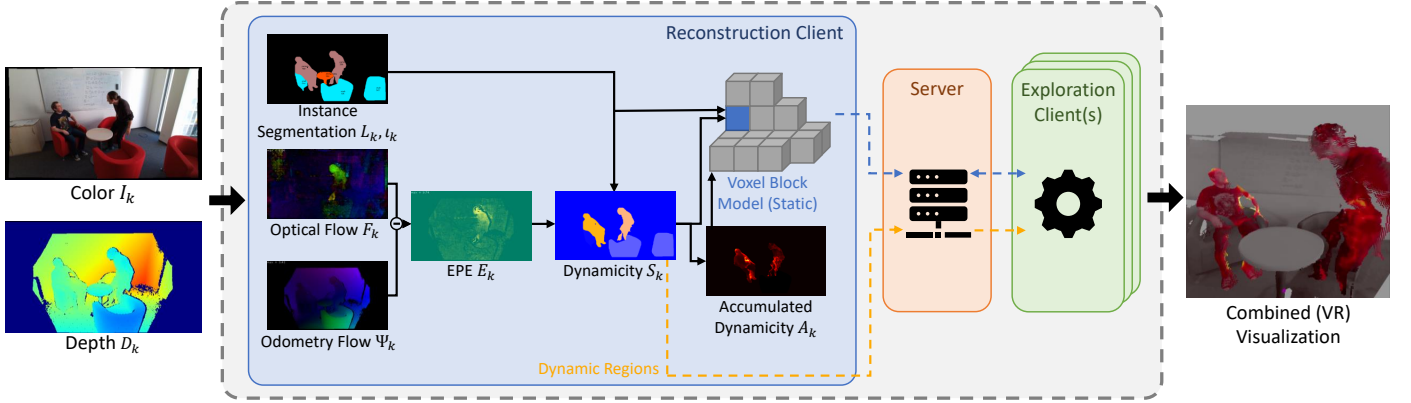


Figure 2: Visualization of different processing stages for the k -th RGB-D frame in the pipeline. Starting with color I_k and depth D_k , instance segmentation L_k (class labels) and t_k (instance IDs), optical flow F_k and odometry flow Ψ_k are computed. Next, the end-point-errors (EPE) between the flows are computed, normalized and propagated using the instance segmentation to generate the dynamicity scores S_k . The scores are accumulated in A_k and L_k, t_k, S_k and A_k are used to integrate information about static regions in the voxel block model. New static voxels and current dynamic regions are sent to the server, which forwards this information to the exploration clients appropriately.

proposals M_1, \dots, M_n which we integrate into the instance and label maps using non-maximum suppression. More specifically, the M_i are represented as Boolean masks that indicate the membership of each pixel, i.e. $M_j(u) = 1$, if pixel u belongs to proposal j , and $M_j(u) = 0$ otherwise. In addition, each mask is associated with a class label l_j and a confidence score $c_j \in [0, 1]$. To produce the per-pixel class label L_k and instance ID maps t_k , we have to integrate potentially overlapping region proposals, taking the confidence scores into account. We accomplish this by first removing proposals with a confidence smaller than a threshold τ_{conf} . For each pixel u , we then find the instance ID of the proposal with maximum confidence, i.e. for the filtered indices j'_1, \dots, j'_n , we compute $i^*(u) = \arg\max_i \{c_i \mid M_i(u) = 1\}$. The resulting assignment is again filtered by removing IDs that do not exceed a minimum pixel count. In other words, we set

$$\hat{i}(u) = \begin{cases} i^*(u), & \text{if } |\{i^*(u) = i\}| \geq \tau_{\text{count}} \\ 0, & \text{otherwise.} \end{cases} \quad (1)$$

The resulting indices are then associated with the IDs from the previous frame to get the final map t_k of instance IDs and the label map is set to the corresponding class labels $L_k(u) = l_{t_k(u)}$. In our experiments, we used YOLOv8 [162] as the segmentation network.

Optical Flow Estimation. Next, we estimate the backward optical flow $F_k = f_{\text{flow}}(I_k, I_{k-1})$, where $F_k(u) \in \mathbb{R}^2$ is the corresponding flow vector at pixel u , such that u in I_k corresponds to $u + F_k(u)$ in I_{k-1} . For f_{flow} , we use the NVIDIA Optical Flow Accelerator (NVOFA) [163]. In order to filter out bad correspondences present in the NVOFA, we additionally compute the forward flow estimate $\bar{F}_k = f_{\text{flow}}(I_{k-1}, I_k)$. The estimator also provides per-pixel costs C_k, \bar{C}_k for the estimates, which we combined with the error between forward and backward flow into a weight map W_k . More specifically, we compute the geometric mean between the three terms

$$W_k = \sqrt[3]{(1 + \|F_k + \bar{F}_k\|_2)^{-1} \cdot (1 + \lambda C_k)^{-1} \cdot (1 + \lambda \bar{C}_k)^{-1}} \quad (2)$$

such that each term lies in the same range $[0, 1]$ and the result represents the level of confidence of the estimate at each pixel. $\lambda \in \mathbb{R}$ is a hyperparameter that scales the cost values of the estimator appropriately.

Odometry. Subsequently, we estimate the camera motion

$$\xi_k = f_{\text{pose}}(I_{k-1}, I_k, D_{k-1}, D_k) \in \mathfrak{se}(3) \quad (3)$$

between the previous and current frame, yielding an absolute camera pose $T_k \in \mathbb{R}^{4 \times 4}$ when we assume T_1 to be centered at the world origin. Our implementation uses a standard point-to-plane RGB-D registration implementation of Open3D [164].

End-point-error. Based on F_k, T_k and W_k , we determine a per-pixel end-point-error E_k between the estimated flow and the flow Ψ_{T_k} we expect from a completely static scene where only the camera is moving by T_k , i.e.

$$E_k(u) = W_k(u) \cdot \|F_k(u) - \Psi_{T_k}(u)\|_2. \quad (4)$$

Using the current depth D_k , we can compute $\Psi_{T_k}(u)$ as the offset between u and the corresponding point u' projected from frame $k-1$ into k . More specifically, let π^{-1} be the backprojection operation, such that $v = \pi^{-1}(u, D_k(u)) \in \mathbb{R}^3$ is the 3D coordinate of pixel u with depth measurement $D_k(u)$ in the local coordinate system of the camera, and let π be the corresponding projection operation transforming v back to u . $\Psi_k(u)$ is then given as

$$\Psi_k(u) = \left[\pi \circ T_{k-1} \circ T_k^{-1} \circ \pi^{-1}(u, D_k(u)) \right] - u. \quad (5)$$

Note that we imply proper conversion between Euclidean and homogeneous coordinates by using the concatenation operator to keep the notation simple.

Dynamicity Score. To decide which of the resulting scores $E_k(u)$ indicate dynamic regions, we found that a simple thresholding is not sufficient, because the average error varies too strongly, especially for frame pairs where the camera tracking

or optical flow network yield poor estimates. To reduce the influence of these fluctuations, we instead analyze the histogram $H^i = (H_1^i, \dots, H_n^i) \in \mathbb{N}^n$ of errors for each instance i . We chose the width c of the n histogram bins empirically as $c = 0.25$ based on the error values produced by our approach. The number of bins is chosen dynamically such that all error values are covered by a bin. As an indicator of the highest motion of i , we look for the rightmost mode $s_k(i) \in \mathbb{R}_{\geq 0}$ of H^i that consists of at least $r_{\text{mode}} \cdot \sum_{l=1}^n nH_l^i$ values, where $r_{\text{mode}} \in [0, 1]$ is a hyperparameter. This means, we look for the bin index $j^*(i)$ with

$$j^*(i) = \max \left\{ j \left| H_{j-1}^i < H_j^i, H_{j+1}^i < H_j^i, \frac{H_j^i}{\sum_l H_l^i} \geq r \right. \right\} \quad (6)$$

which, in turn, allows the mode m_i to be defined as the center of the histogram bin $j^*(i)$, i.e. $s_k(i) = (j^*(i) + 0.5)c$.

We normalize all scores by subtracting the smallest mode from them, assuming that at least one of the detections is of static nature. Together with an empirically chosen linear rescaling by a factor $\delta \in \mathbb{R}_{>0}$, we get the normalized scores

$$E'_k(u) = \delta \cdot (E_k(u) - \min_i \{s_k(i)\}) \quad (7)$$

which fulfill the previously mentioned criterion that scores $S_k(u) \leq 1$ are indicating a static object, while higher scores indicate dynamic regions.

While $E'_k(u)$ can now be used for the segmentation into static and dynamic regions, we found the visualization of moving regions to be more coherent if the segmentation happens on the object level. This is particularly important for articulated or non-rigid objects like humans, where potentially only a small part of the object (e.g. an arm) is moving. To accomplish this, we use the normalized modes $s'_k(i)$, which result from applying the transformation from Equation (7) to m_i . An instance i is deemed as dynamic if $s'_k(i) \geq \tau$. To represent this in the resulting score map, we propagate this value in the final score map by setting $S_k(u) = s'_k(i)$ for all pixels u with $\iota_k(u) = i$.

Temporal Smoothing. To make the dynamicity estimates more robust against noise in the error values when looking at multiple frames, we experimented with smoothing the values $s'_k(i)$ temporally using the maximum over the current and a decaying previous score, such that the smoothed score of instance i in frame k is given as

$$\hat{s}'_k(i) := \max\{\alpha \cdot \hat{s}'_{k-1}(i), s'_k(i)\}. \quad (8)$$

To make this work, we have to re-identify instance i from frame $k-1$ in frame k . A priori, instance IDs do not have any relation to each other, because f_{seg} is assumed to only be dependent on a single image. We use information about the mask overlap between ι_k, L_k and ι'_{k-1}, L'_{k-1} , where the latter maps result from warping ι_{k-1}, L_{k-1} according to the flow F_k , aligning them with the maps of frame k . A confusion matrix C of the pairwise overlaps of the instance masks of the same class in ι_k and ι'_{k-1} is computed, such that

$$C_{ij} = |\{u \mid \iota_k(u) = i, \iota'_{k-1}(u) = j, L_k(u) = L'_{k-1}(u)\}|. \quad (9)$$

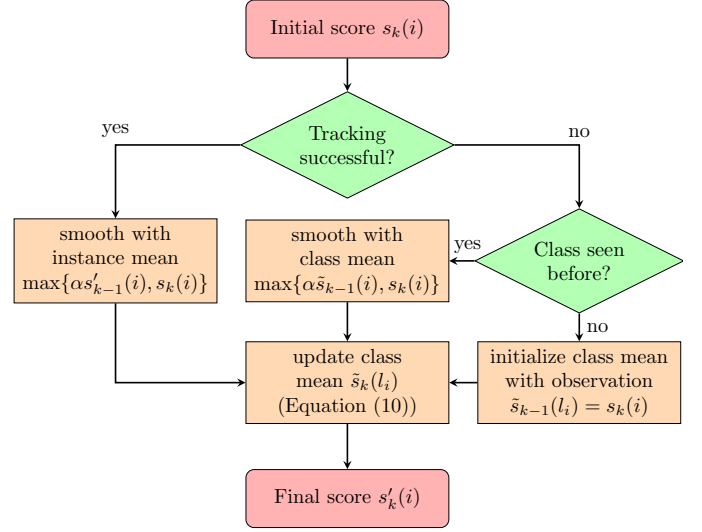


Figure 3: Flowchart visualizing the procedure for the temporal smoothing of the dynamicity score of instance i with class label l_i in frame k . If the tracking matches instance i with an instance from the previous frame, the resulting score is smoothed as shown in Equation (6). Otherwise, we first check whether the class was observed in a previous frame. In this case, we smooth the score similarly to Equation (6) but using the smoothed class mean from the last frame instead. In case the class is observed for the first time, we keep the initial score and use it as the new class mean for l_i . Lastly, the class mean for l_i is updated.

We identify instance i with instance j' from the previous frame, if $j' = \operatorname{argmax}_j \{C_{ij'}\}$ and $C_{ij'}$ is larger than a minimum overlap ratio $r_{\text{track}} \in [0, 1]$. For instances that cannot be associated with an instance in the previous frame, we keep a mean for the dynamicity scores of each class that is smoothed according to the scheme shown in Equation (7). More specifically, let $\tilde{s}_k : \mathcal{L} \rightarrow \mathbb{R}_{\geq 0}$ be defined as a mapping from the set of class labels \mathcal{L} to the mean dynamicity scores, where

$$\tilde{s}_k(l) := \max \left\{ \alpha_{\text{class}} \cdot \tilde{s}_{k-1}(l), \frac{1}{|I_l|} \sum_{i \in I_l} \hat{s}'_k(i) \right\}. \quad (10)$$

Figure 3 depicts the steps taken to compute the temporally smoothed score $s'_k(i)$ of some instance i with label l_i from the initial score $s_k(i)$. Importantly, we also handle the case that a class is observed for the first time in the current frame where we set the class mean to the only available observation $s_k(i)$.

Score Accumulation. As the object tracking is only performed in 2D for efficiency reasons, we also accumulate the dynamicity scores of each instance over time in 2D by updating an accumulation map $A_k(u) \in \mathbb{R}_{\geq 0}$. To increase the interpretability of the scores, we compute a 3D end-point-error between the last and current frame by using F_k for the correspondences between the pixels and backprojecting the respective coordinates of into 3D using π^{-1} with the corresponding depth maps and camera poses. The resulting 3D flow $\hat{F}_k(u) \in \mathbb{R}^3$ is then combined with the warped previous accumulated score A'_{k-1} to $A_k(u) = A'_{k-1}(u) + \|\hat{F}_k(u)\|_2$. We also experimented to use \hat{F}_k as an input for the end-point-error calculation, but found that the signal was too noisy for our method to be used in that way.

3.2. Update of the Static Model

With the score map S_k computed, we are able to integrate the static part of the frame into the static model. For this purpose, we use a modified version of real-time 3D reconstruction based on spatial voxel block hashing [69], where we added an extension for concurrent retrieval, insertion and removal of data [27]. However, in order to further increase the efficiency of our approach, we seamlessly shift potentially dynamic but currently static scene parts into the static scene representation until they become dynamic again. This requires us to additionally consider the following situations:

1. Dynamic regions should not be integrated into the static model. In case this happens erroneously, they should be removed as quickly as possible.
2. Regions that change their state from dynamic to static (e.g. a box was placed on a table) should be integrated into the static model seamlessly.
3. Regions changing their state from static to dynamic (e.g. a box is picked up) should be removed from the static model immediately.
4. Static regions that changed while not in the camera frustum should be updated as soon as new information is available.

Following the suggested modification of the weighting schema for dynamic object motion by Newcombe et al. [67], we truncate the updated weight which effectively results in a moving average favoring newer measurements. However, instead of applying a global maximum weight $W_\eta > 0$, we store a separate value $W_{\eta,k}(v) > 0$ for each voxel v in our model and compute the new weight $W_k(p) \in \mathbb{R}_{\geq 0}$ as

$$W_k(v) = \min(W_{k-1}(v) + W'_k(v), W_{\eta,k}). \quad (11)$$

These maximum weights are computed directly from the dynamicity score. We found that a simple step function leads to good results, i.e.

$$W_{\eta,k}(v) = \begin{cases} \hat{W}_\eta, & S_k(u_v) \leq \tau_\eta \\ \check{W}_\eta, & S_k(u_v) > \tau_\eta \end{cases}, \quad (12)$$

given the corresponding raycasting source pixel $u_v \in \mathcal{U}$ of voxel v , a threshold $\tau_\eta > 0$ and weight caps $0 < \check{W}_\eta \leq \hat{W}_\eta$. This helps in situations 1 and 3, since dynamic regions are updated with new information more quickly, as well as in situation 4, as the weight is truncated even for static regions.

In addition, we aid the timely removal of dynamic regions from the static model (situations 1 and 3) by setting the SDF value to -1 for voxels where the associated dynamicity score $S_k(p)$ exceeds a threshold $\tau_{\text{SDF}} > 0$. In conjunction with the high integration weight from before, this invalidates the existing surface estimate at that location.

Situation 2 is already covered by the temporal smoothing of the dynamicity scores in Equation (8), because the decay parameter α prevents to drop the scores too quickly, which leads to objects being considered dynamic for some time when they

stop moving. Even though it takes a short time for the static reconstruction to integrate and stream the voxels of the state-changing object, we found this to be more intuitive when observing the live scene to have the object stop first than to suddenly disappear.

3.3. Visualization

After having streamed the hybrid scene representation to remote users' devices, the static and dynamic scene entities have to be combined within an immersive scene exploration component, where we focus on VR-based immersion of users into the live-captured scenarios. For this, we created a client component that receives updates of the static model as well as the dynamic regions of the current RGB-D frame.

The static model is visualized as a mesh, where the local mesh representation of the static scene is updated using received MC voxel block indices and rendered in real time, thereby following previous work [27]. In contrast, the dynamic parts are shown as a point cloud at the corresponding location relative to the static mesh. For this, we backproject the dynamic pixels of the current RGB-D frame using the known camera intrinsics and the current camera pose.

The user is then able to individually and independently from the sensor explore the captured scene by physically looking and walking around or use a teleportation functionality for locomotion. The current position and orientation of the RGB-D sensor and other users is also shown.

3.4. Streaming

To be able to run the described method with low latency from the time of capturing to the visualization at remote locations, we use a server-client architecture. The server receives and distributes data packages over a network to the appropriate processing clients. The RGB-D capture, segmentation into static and dynamic regions as well as the integration into the static model are performed in the *reconstruction client*.

Updates of this representation are then broadcasted to one or multiple *exploration clients*, which in turn update a mesh representation of the static scene using the MC indices. At the same time, the server also sends updates of the dynamic regions as masked RGB-D images together with the current camera pose estimate, such that the RGB-D pixels can be projected into the scene as a point cloud.

For all network communication, we use a general-purpose lossless data compression scheme [165] to reduce the bandwidth requirements.

3.5. Implementation Details

To take advantage of modern multi-processor architectures, the stages shown in Figure 2 are running concurrently, such that each stage can start with the next item once the processing of the current one has been completed. While this leads to overhead due to inter-process communication, the FPS of the pipeline is no longer bound to the latency, but the processing duration of the slowest stage in the pipeline. This can also be observed in our detailed performance evaluation in Figure 6.

Symbol	Description	Value
τ_{conf}	Min. segmentation confidence	0.2
τ_{count}	Min. pixel count for class acceptance	2300
τ	Dynamic threshold	1.2
τ_{η}	Voxel weight dynamicity threshold	1.2
τ_{SDF}	SDF invalidation threshold	1.2
\hat{W}_{η}	Static max. voxel weight	255
\check{W}_{η}	Dynamic max. voxel weight	3
c	Histogram bin width	0.05
r_{mode}	Histogram relative min. bin count	0.01
r_{track}	Instance tracking min. overlap ratio	0.2
α	Instance dynamicity decay factor	0.99
α_{class}	Class dynamicity decay factor	0.99
δ	Dynamicity norm. scale factor	0.01
λ	NVOFA cost buffer scale factor	0.03

Table 1: Choices for the hyperparameters of the pipeline used for all sequences during the evaluation.

Scene	F.	M.	O.	end-to-end [s]	FPS [1/s]
items_1	✓			0.40 (0.02)	18.95 (5.75)
items_2	✓			0.40 (0.03)	18.67 (5.95)
people_1	✓			0.39 (0.02)	19.33 (5.94)
people_2		✓		0.41 (0.03)	17.92 (5.12)
people_3		✓		0.43 (0.03)	17.73 (4.81)
people_4		✓		0.40 (0.03)	17.98 (5.34)
people_5		✓		0.40 (0.02)	19.01 (5.64)
ego_view		✓		0.40 (0.02)	18.93 (5.79)
oof_1			✓	0.40 (0.08)	19.81 (6.05)
oof_2			✓	0.40 (0.02)	19.56 (6.39)

Table 2: Performance results on the 10 self-recorded scenes. The F., M., O. columns indicate the type of motion that was captured (F: fixed camera when object motion is seen, M: camera always in motion, O: static scene manipulation outside of camera view). Latency and FPS columns show both the mean and standard deviation (in parentheses) of the respective metrics.

4. Experimental Results

To evaluate the performance of the proposed pipeline, we ran experiments on 10 self-recorded sequences captured with a Microsoft Azure Kinect RGB-D sensor in different office environments, and measured both speed and bandwidth metrics.

The scenes contain varying types of motion and we categorized them into three groups. Fixed (F.) are scenes that have no camera motion once dynamic entities can be seen in the camera, whereas Moving (M.) describes scenes with an always-moving camera and simultaneous object motion. A third category Outside (O.) contains a scene where the camera is hand-held, but object motion only happens outside of the camera view. A short description and some exemplary images of each scene are shown in Table 4.

To validate design choices, we also conducted an ablation study regarding certain components of the pipeline and compared them to baseline methods. Following that, we will dis-

Type	F.	M.	O.
TSDF	44.80 (77.90)	69.72 (92.14)	65.70 (81.21)
MC	3.89 (6.13)	6.10 (7.31)	6.30 (5.83)
Dyn.	7.06 (7.37)	7.41 (8.43)	2.66 (4.42)

Table 3: Required mean bandwidth and respective standard deviation (in parentheses) in MBit/s of the different types of data packages over the types of recorded scenes (F: fixed camera when object motion is seen, M: camera always in motion, O: object motion only outside of camera view).

cuss the impact and limitations of the approach.

4.1. Experimental Setup

We set up three computers in a local network that each run one of the three processes shown in Figure 2. All devices use the same hardware except for the GPU, which is an Nvidia GeForce RTX 3090 for the reconstruction client and an Nvidia GeForce GTX 1080 for both server and exploration client, as they require less GPU performance. The hyperparameters used for the performance evaluation and visualization were fixed for all scenes and are listed in Table 1.

We measured three different metrics in this setup: The end-to-end latency of an RGB-D frame from the camera to the exploration client, the frame-rate at which RGB-D frames are being processed by the components of the pipeline, and the network bandwidth between server and connected clients. The latency and frame-rate is measured using timestamped logs that are synchronized between all computers to ensure a minimal deviation for the timesteps that is bound by the local network latency. The frame-rate is given as the averaged arrival time difference between consecutive dynamic RGB-D images at the exploration client and the latency is the average between the emission times of RGB-D frames into the pipeline and the corresponding arrival times at the exploration client.

4.2. Evaluation of Performance and Visual Quality

Table 2 shows the results of the frame-rate and latency measurements. Here, the performance is largely independent of the type of scene and exhibits an average of around 0.4 seconds in end-to-end latency and a frame-rate of 18.8 frames per second (FPS). A closer analysis reveals that the frame-rate is upper-bound by the single image inference speed of the instance segmentation network. In Table 6, we list the raw computation speed of individual components of our pipeline during evaluation. Note that the components run in parallel, so the actual processing speed of each component is limited by the output speed of the previous one. The measured values therefore only represent a lower bound for the execution speed that each component can reach in our implementation. An example of this parallel execution is also visualized in Figure 6.

The network bandwidth requirements are summarized in Table 3. Here, the measured package sizes are split up in the type of data. TSDF represents the values of the truncated signed-distance function generated by the voxel block hashing of the reconstruction client, MC labels the Marching Cubes indices the server generates from the TSDF representation and sends




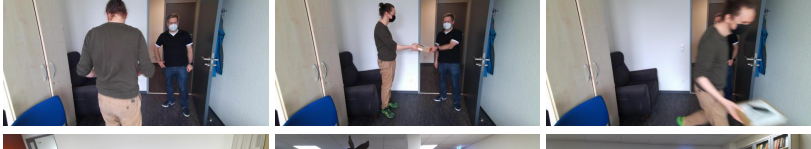
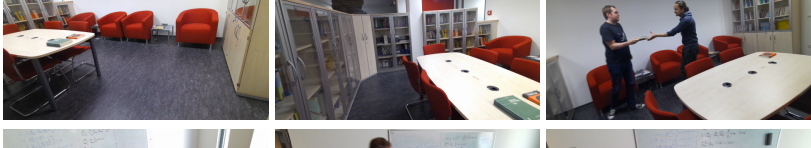
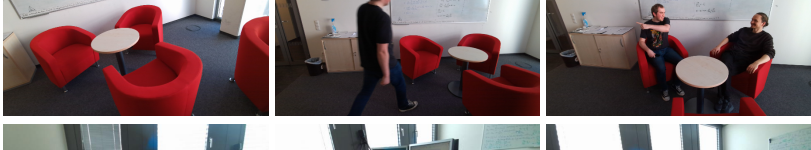
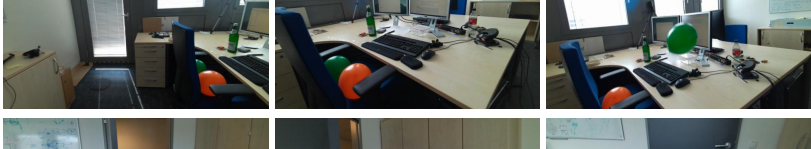


Scene	Description	Exemplary Images from Scene
items_1	A person moves around items (books and boxes) on an office table.	
items_2	A person picks up and drops off items on a table in a medium-sized office.	
people_1	Two persons meet at a coffee table and exchange a box.	
people_2	Chairs and a boxes are moved around in an office seating area.	
people_3	Two persons exchange a small box.	
people_4	Two persons meet in a library corner and exchange books.	
people_5	Two persons briefly meet and talk in a seating area.	
ego_view	Balloons are kicked around in a medium-sized office.	
oof_1	An office door is moved once while seen by the camera and once unseen.	
oof_2	A box is moved multiple times while the camera is not observing it.	

Table 4: Short description and exemplary images for each of the scenes used for the evaluation.

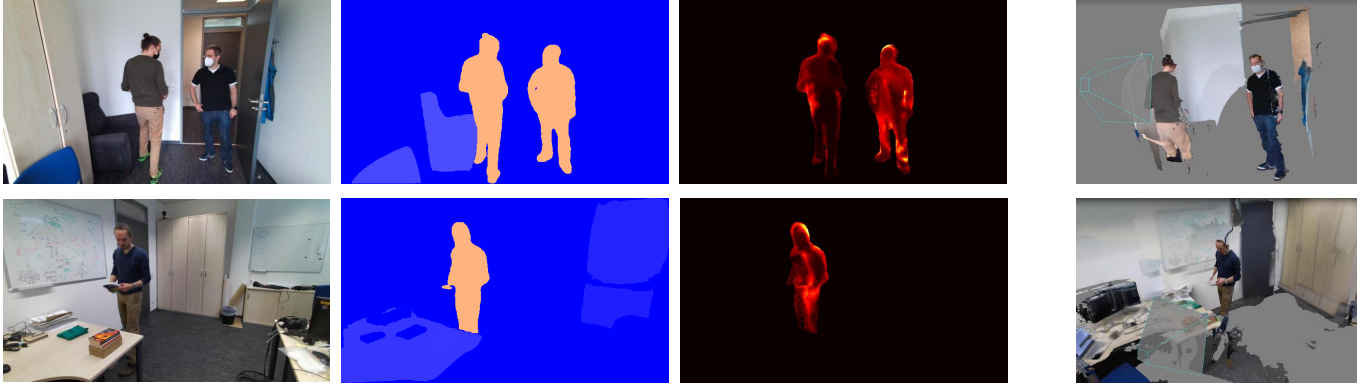


Figure 4: Results of our approach on different scenes. Left to right: Input color image; resulting segmentation into static (blue) and dynamic (yellow) regions; the accumulated 3D flow magnitude; a novel view of the scene as visualized in the exploration client.

Segmentation	Optical Flow	FPS [1/s]
SCNet [166]	NVOFA [163]	4.47 (0.36)
PointRend [167]		6.60 (0.66)
Mask R-CNN [168]		8.04 (1.09)
SoloV2 [169]		14.95 (5.31)
YoloV8 [162]	GMA [170]	2.75 (0.11)
	RAFT [171]	3.02 (1.04)
	MaskFlowNet [172]	9.45 (1.17)
	LiteFlowNet2 [173]	13.69 (3.10)
YoloV8 [162]	NVOFA [163]	18.95 (5.75)

Table 5: Performance comparison of our pipeline using different approaches for instance segmentation and optical flow on the scene *items_1*. For this purpose, we provide the resulting frame-rate (standard deviation) our approach reaches using the given combinations of networks.

to the exploration client(s). The dynamic RGB-D that results from the segmentation of the reconstruction client and that is subsequently sent to the exploration client(s) is called Dyn. The results indicate that the majority of data is transferred between reconstruction client and server. The Marching Cubes indices and dynamic RGB-D data, which are selectively streamed to the exploration client(s), allow for multiple connections, even over the Internet, considering modern bandwidth availability. Furthermore, we provide qualitative results in Figure 4.

4.3. Ablation Study

To validate some of the design choices of our approach, we show the effects of removing certain elements of the pipeline on the results. Figure 5 illustrates the effect of the weighting function from Equation (12) as well as the difference between error thresholding with and without propagation into the object masks. In the weighting example, we show that the update of inconsistent measurements results in less artifacts while walking around the box when using an exponential decay. This motivates our choice to enable this weighting schema for regions with recent object motion. At the same time, the floor texture shows slightly more artifacts as the more recent measurements

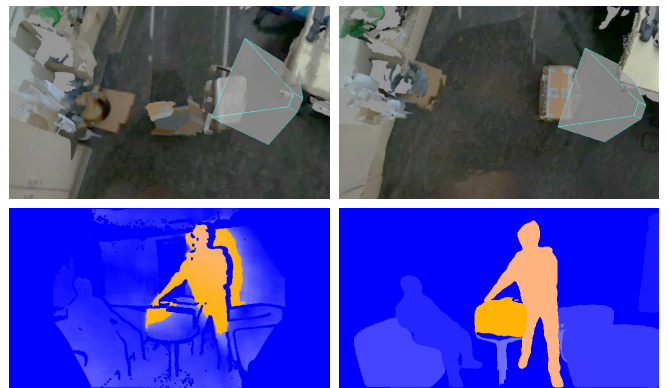


Figure 5: Comparison of design choices of the proposed pipeline. Top row: An example output from the exploration client using the standard voxelblock weighting schema (left) vs. exponential weight decay via weight capping. The second approach yields a reconstruction of the box with less artifacts. Bottom row: Thresholding of the normalized EPE before (left) and after (right) propagation of the error modes into the static (blue) and dynamic (yellow) object masks. Again, the second approach produces a more plausible segmentation into static and dynamic regions.

are favored, but collide visually with regions that were not recently seen by the camera. This effect is reduced in the original weighting schema, which motivates the dual approach shown in Equation (12).

The bottom row of Figure 5 shows how the propagation of the error modes into the object masks aids to correctly identify potentially dynamic objects. Due to weak motion boundaries produced by f_{flow} , a large region of pixels behind the moving person is considered dynamic after normalization. This can be filtered out completely in this case using our approach.

4.4. Comparison with Further Segmentation and Optical Flow Networks

To evaluate the choice of the instance segmentation network [162] and optical flow estimation [163] used in our approach, we compared the performance differences with some other recent segmentation [166–169] and optical flow [170–173] techniques. Table 5 shows our pipeline’s performance in terms of frames per second when replacing either the segmentation or

Scene Test	System Components							Voxel Hashing
	Odometry	Optical Flow	Segmentation		Dynamicity			
			Inference	Tracking	EPE	Postproc.	Acc.	
items_1	24.55	28.40	42.95	15.00	26.60	21.75	25.75	33.45
items_2	21.80	28.80	44.70	13.60	25.70	19.80	25.10	38.60
people_1	24.10	28.70	42.45	14.90	25.80	19.80	25.55	34.05
people_2	24.80	29.20	44.70	15.90	26.60	21.00	26.00	43.30
people_3	25.20	29.60	45.10	16.40	26.90	20.80	26.70	46.10
people_4	22.55	29.05	46.20	15.75	26.10	20.85	26.20	41.35
people_5	25.10	28.53	41.97	14.47	26.10	19.80	25.30	40.90
ego_view	24.85	28.55	43.20	14.65	25.95	20.20	25.75	39.95
oof_1	24.30	28.90	38.25	12.20	25.15	18.85	24.75	41.00
oof_2	22.10	28.60	40.60	12.70	26.20	18.75	25.05	39.70
mean	23.94	28.83	43.01	14.56	26.11	20.16	25.62	39.84

Table 6: Raw computation speeds in milliseconds for the major components of our pipeline, evaluated separately for each of the 10 scenes used for the evaluation. The last row shows the mean over all scenes. The dynamicity computation is split into end-point-error computation (EPE), postprocessing (Postproc., which includes normalization, temporal smoothing, and object propagation), accumulation (Acc.) and updating the static model (Voxel Hashing).

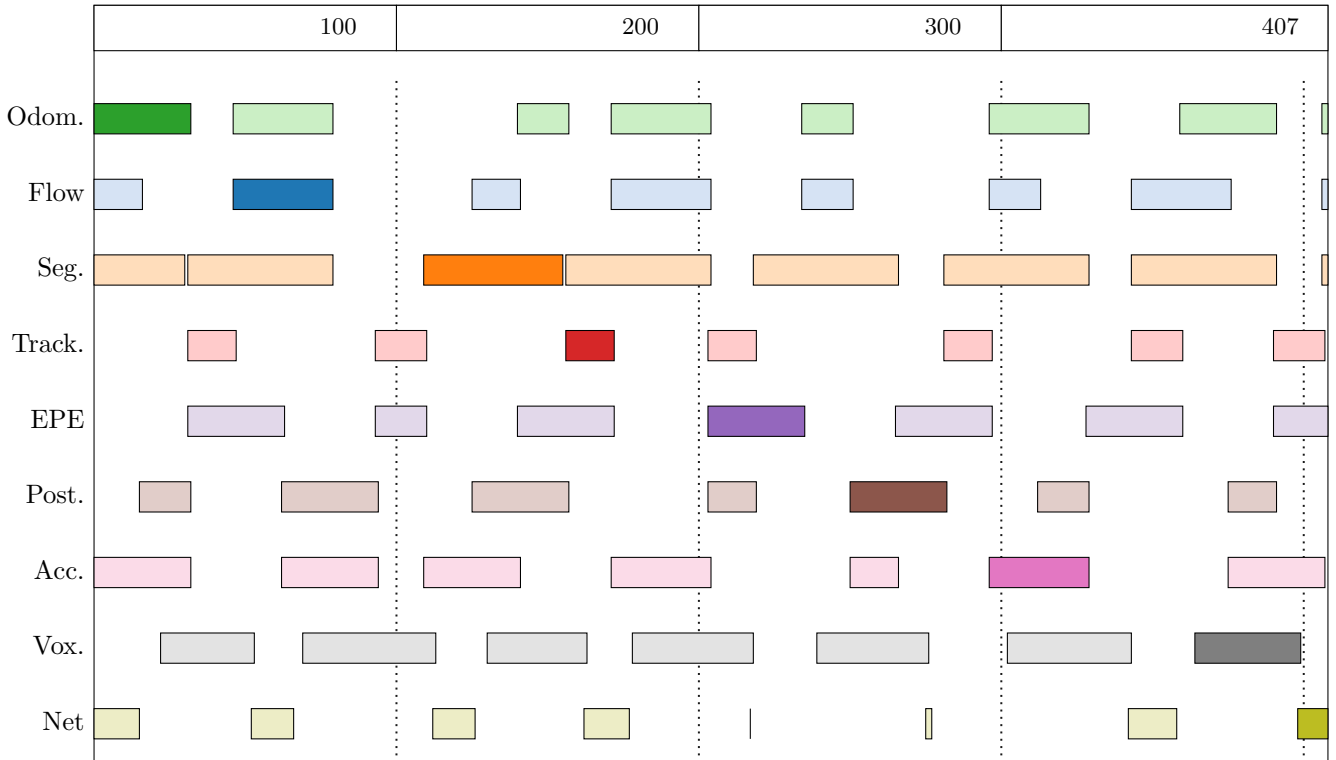


Figure 6: Gantt chart showing the compute durations of the major components of our pipeline on a single frame from arriving at the first process of the pipeline (0ms) to being received at the exploration client (407ms) from the evaluation of scene *items_1*. The highlighted bars correspond to the observed frame. System components are odometry (Odom.), optical flow estimation (Flow), instance segmentation (Seg.), instance tracking (Track.), end-point-error computation (EPE), dynamicity postprocessing (Post.), dynamicity accumulation (Acc.), integration into the static model (Vox.) and network latency (Net.). It can be seen that faster components of the pipeline have to wait for the next frame to become available to continue processing. Additional gaps result from scheduling and process communication.

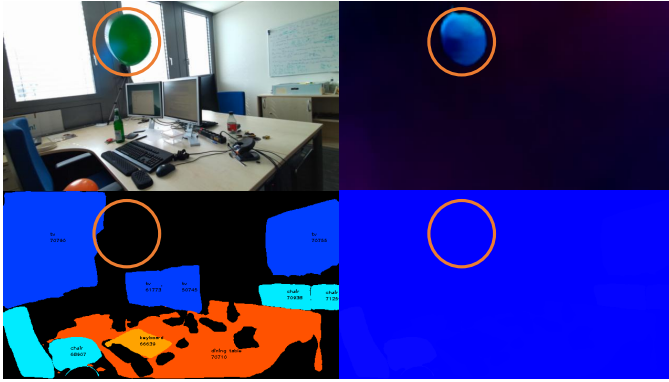


Figure 7: Failure case of our method. Shown are RGB (top left), optical flow (top right), instance segmentation (bottom left) and resulting segmentation into static and dynamic (bottom right). Even though a clear motion cue is available in the optical flow image, due to a missing object detection, our method fails to correctly identify the dynamic region (orange circle).

the optical flow approach. It can be seen that the combination we chose (bottom row) yields the highest processing speed.

4.5. Limitations

While our approach shows promising results and is designed with modularity and extensibility in mind, there are also some limitations to consider. Most importantly, the pipeline only runs at frame-rates close to real-time due to the performance limitations inherited by the involved neural network approaches. In our scenario, we require high single-image inference speed, which is not a functionality modern deep learning approaches are particularly tuned for. Furthermore, our approach requires the segmentation network to detect objects to be able to identify dynamic regions, which limits its capabilities on out-of-distribution samples. Objects not detected by the instance segmentation network affect their assignment to the static or dynamic scene parts, which is shown in Figure 7. Here, the balloon is not detected as an object by the segmentation network and is therefore erroneously integrated into the static model. While the integrated voxels conflict with future measurements and are eventually removed, they cause visually unpleasant artifacts during reconstruction. This is also the case for the optical flow network, as it is also limited by the quality of the training data and the domain overlap with the scenes we recorded. However, due to the modular nature of our approach, future developments with improved accuracy of the predictions might address this current limitation of our approach. Furthermore, future developments on increasing the efficiency of the networks for the respectively involved subtasks will further improve the overall performance.

5. Conclusions

We presented a novel live-telepresence system that allows immersing remote users into live-captured environments with static and dynamic scene entities beyond an area of a few square-meters at practical bandwidth requirements. In order to allow the respectively required efficient 3D reconstruction,

data streaming and VR-based visualization, we built our system upon a novel hybrid volumetric scene representation that combines a voxel-based representation of static scene geometry enriched by additional information regarding object semantics as well as their accumulated dynamic movement over time with a point-cloud-based representation for dynamic parts, where we perform the respective separation of static and dynamic parts based on optical flow and instance information extracted for the input frames. As a result of independently yet simultaneously streaming static and dynamic scene characteristics while keeping potentially moving but currently static scene entities in the static model as long as they remain static, as well as their fusion in the visualization on remote client hardware, we achieved VR-based live-telepresence in large-scale scenarios at close to real-time rates.

With the rapid improvements in hardware technology, particularly regarding GPUs, we expect our system to soon reach full real-time capability. Also, the modularity of our system allows replacing individual components with newer approaches, which might be particularly relevant for the instance segmentation network as it represents the main bottleneck of our current system.

Acknowledgements

This work was supported by the DFG project KL 1142/11-2 (DFG Research Unit FOR 2535 Anticipating Human Behavior) and NFDI4Culture (DFG Project Number 441958017).

References

- [1] M. Minsky, Telepresence, *Omni* 2 (9) (1980) 44–52. [1](#)
- [2] G. Fontaine, The experience of a sense of presence in intercultural and int. encounters, *Presence: Teleoper. Virtual Environ.* 1 (4) (1992) 482–490.
- [3] R. Held, Telepresence, *The Journal of the Acoustical Society of America* 92 (4) (1992) 2458–2458. [doi:10.1121/1.404500](#).
- [4] B. G. Witmer, M. J. Singer, Measuring presence in virtual environments: A presence questionnaire, *Presence: Teleoper. Virtual Environ.* 7 (3) (1998) 225–240.
- [5] J. V. Draper, D. B. Kaber, J. M. Usher, Telepresence, *Human factors* 40 (3) (1998) 354–375. [1](#)
- [6] J. Steuer, Defining virtual reality: Dimensions determining telepresence, *Journal of communication* 42 (4) (1992) 73–93. [1](#)
- [7] D. W. Schloerb, A quantitative measure of telepresence, *Presence: Teleoperators & Virtual Environments* 4 (1) (1995) 64–80. [1](#)
- [8] S. J. Gibbs, C. Arapis, C. J. Breiteneder, Teleport-towards immersive copresence, *Multimedia Systems* 7 (3) (1999) 214–221. [doi:10.1007/s005300050123](#). [1](#)
- [9] L. Muhlbach, M. Bocker, A. Prussog, Telepresence in videocommunications: A study on stereoscopy and individual eye contact, *Human Factors* 37 (2) (1995) 290–305. [1](#)
- [10] M. Gross, S. Würmlin, M. Naef, E. Lamboray, C. Spagno, A. Kunz, E. Koller-Meier, T. Svoboda, L. Van Gool, S. Lang, et al., blue-c: a spatially immersive display and 3d video portal for telepresence, *ACM Transactions on Graphics (TOG)* 22 (3) (2003) 819–827. [doi:10.1145/882262.882350](#). [1, 2](#)
- [11] R. Vasudevan, G. Kurillo, E. Lobaton, T. Bernardin, O. Kreylos, R. Bajcsy, K. Nahrstedt, High-quality visualization for geographically distributed 3-d teleimmersive applications, *IEEE Trans. on Multimedia* 13 (3) (2011) 573–584. [doi:10.1109/tmm.2011.2123871](#).

- [12] A. Maimone, H. Fuchs, Encumbrance-free telepresence system with real-time 3d capture and display using commodity depth cameras, in: Proc. of the IEEE Int. Symp. on Mixed and Augmented Reality, IEEE, 2011, pp. 137–146. doi:10.1109/ismar.2011.6092379.
- [13] A. Maimone, J. Bidwell, K. Peng, H. Fuchs, Enhanced personal autostereoscopic telepresence system using commodity depth cameras, Computers & Graphics 36 (7) (2012) 791 – 807. doi:10.1016/j.cag.2012.04.011. 2
- [14] A. Collet, M. Chuang, P. Sweeney, D. Gillett, D. Evseev, D. Calabrese, H. Hoppe, A. Kirk, S. Sullivan, High-quality streamable free-viewpoint video, ACM Transactions on Graphics (ToG) 34 (4) (2015) 1–13. doi:10.1145/2766945.
- [15] D. J. Roberts, A. J. Fairchild, S. P. Champion, J. O’Hare, C. M. Moore, R. Aspin, T. Duckworth, P. Gasparello, F. Tecchia, withyou—an experimental end-to-end telepresence system using video-based reconstruction, IEEE Journal of Selected Topics in Signal Processing 9 (3) (2015) 562–574. doi:10.1109/jstsp.2015.2402635.
- [16] A. J. Fairchild, S. P. Champion, A. S. García, R. Wolff, T. Fernando, D. J. Roberts, A mixed reality telepresence system for collaborative space operation, IEEE Trans. on Circuits and Systems for Video Technology 27 (4) (2016) 814–827. doi:10.1109/tcsvt.2016.2580425.
- [17] N. Zioulis, D. Alexiadis, A. Doumanoglou, G. Louizis, K. Apostolakis, D. Zarpalas, P. Daras, 3d tele-immersion platform for interactive immersive experiences between remote users, in: 2016 IEEE International conference on image processing (ICIP), IEEE, IEEE, 2016, pp. 365–369. doi:10.1109/icip.2016.7532380.
- [18] S. Orts-Escolano, et al., Holoportation: Virtual 3d teleportation in real-time, in: J. Rekimoto, T. Igarashi, J. O. Wobbrock, D. Avrahami (Eds.), Proc. of the Annual Symp. on User Interface Software and Technology, ACM, 2016, pp. 741–754. doi:10.1145/2984511.2984517.
- [19] M. Joachimczak, J. Liu, H. Ando, Real-time mixed-reality telepresence via 3d reconstruction with hololens and commodity depth sensors, in: E. Lank, A. Vinciarelli, E. E. Hoggan, S. Subramanian, S. A. Brewster (Eds.), Proceedings of the 19th ACM International Conference on Multimodal Interaction, ACM, 2017, pp. 514–515. doi:10.1145/3136755.3143031.
- [20] R. Komiya, T. Miyaki, J. Rekimoto, Jackin space: designing a seamless transition between first and third person view for effective telepresence collaborations, in: P. Mistry, P. Maes, J.-M. Seigneur, S. Nanayakkara, J. Paradiso (Eds.), Proceedings of the 8th Augmented Human International Conference, ACM, 2017, pp. 1–9.
- [21] P.-C. Su, J. Shen, M. U. Rafique, Rgb-d camera network calibration and streaming for 3d telepresence in large environment, in: 2017 IEEE Third International Conference on Multimedia Big Data (BigMM), IEEE, IEEE, 2017, pp. 362–369. doi:10.1109/bigmm.2017.83.
- [22] R. Du, M. Chuang, W. Chang, H. Hoppe, A. Varshney, Montage4d: interactive seamless fusion of multiview video textures, in: S. N. Spencer, M. McGuire, D. Nowrouzezahrai (Eds.), Proceedings of ACM SIGGRAPH Symposium on Interactive 3D Graphics and Games (I3D), ACM, 2018, pp. 5:1–5:11. doi:10.1145/3190834.3190843.
- [23] V. Parikh, M. Khara, A mixed reality workspace using telepresence system, in: International Conference on ISMAC in Computational Vision and Bio-Engineering, Springer, Springer International Publishing, 2018, pp. 803–813. doi:10.1007/978-3-030-00665-5_78.
- [24] D.-M. Córdova-Esparza, J. R. Terven, H. Jiménez-Hernández, A. Herrera-Navarro, A. Vázquez-Cervantes, J.-M. García-Huerta, Low-bandwidth 3d visual telepresence system, Multimedia Tools and Applications 78 (15) (2019) 21273–21290. doi:10.1007/s11042-019-7464-0.
- [25] J. Lawrence, D. B. Goldman, S. Achar, G. M. Blascovich, J. G. Desloge, T. Fortes, E. M. Gomez, S. Häberling, H. Hoppe, A. Huibers, C. Knaus, B. Kuschak, R. Martin-Brualla, H. Nover, A. I. Russell, S. M. Seitz, K. Tong, Project starline: A high-fidelity telepresence system, ACM Transactions on Graphics (Proc. SIGGRAPH Asia) 40(6) (2021) 242:1–242:16. doi:10.1145/3478513.3480490. 1, 2
- [26] A. Mossel, M. Kröter, Streaming and exploration of dynamically changing dense 3d reconstructions in immersive virtual reality, in: E. E. Veas, T. Langlotz, J. Martínez-Carranza, R. Grasset, M. Sugimoto, A. Martín (Eds.), Proc. of IEEE Int. Symp. on Mixed and Augmented Reality, IEEE, 2016, pp. 43–48. doi:10.1109/ismar-adjunct.2016.0035. 1, 2, 3
- [27] P. Stotko, S. Krumpfen, M. B. Hullin, M. Weinmann, R. Klein, Slamcast: Large-scale, real-time 3d reconstruction and streaming for immersive multi-client live telepresence, IEEE Transactions on Visualization and Computer Graphics 25 (5) (2019) 2102–2112. doi:10.1109/tvcg.2019.2899231. 2, 3, 6
- [28] P. Stotko, S. Krumpfen, M. Weinmann, R. Klein, Efficient 3d reconstruction and streaming for group-scale multi-client live telepresence, in: 2019 IEEE International Symposium on Mixed and Augmented Reality (ISMAR), IEEE, 2019, pp. 19–25. doi:10.1109/ismar.2019.00018. 2, 3
- [29] P. Stotko, S. Krumpfen, M. Schwarz, C. Lenz, S. Behnke, R. Klein, M. Weinmann, A vr system for immersive teleoperation and live exploration with a mobile robot, in: 2019 IEEE/RSJ International Conference on Intelligent Robots and Systems (IROS), IEEE, IEEE, 2019, pp. 3630–3637. doi:10.1109/iros40897.2019.8968598. 2
- [30] P. Stotko, S. Krumpfen, R. Klein, M. Weinmann, Towards scalable sharing of immersive live telepresence experiences beyond room-scale based on efficient real-time 3d reconstruction and streaming, in: CVPR Workshop on Computer Vision for Augmented and Virtual Reality, 2019. 1, 2, 3
- [31] H. Fuchs, G. Bishop, K. Arthur, L. McMillan, R. Bajcsy, S. Lee, H. Farid, T. Kanade, Virtual space teleconferencing using a sea of cameras, in: Proc. of the Int. Conf. on Medical Robotics and Computer Assisted Surgery, 1994, pp. 161 – 167. 2
- [32] T. Kanade, P. Rander, P. J. Narayanan, Virtualized reality: constructing virtual worlds from real scenes, IEEE MultiMedia 4 (1) (1997) 34–47. doi:10.1109/93.580394.
- [33] J. Mulligan, K. Daniilidis, View-independent scene acquisition for telepresence, in: Proc. IEEE and ACM Int. Symp. on Augmented Reality, IEEE, 2000, pp. 105–108. doi:10.1109/isar.2000.880933.
- [34] H. Towles, W. Chen, R. Yang, S. Kum, H. Fuchs, N. Kelshikar, J. Mulligan, K. Daniilidis, C. C. Hill, L. Holden, B. Zeleznik, A. Sadagic, J. Lanier, 3d tele-collaboration over internet2, in: Proc. of the Int. Workshop on Immersive Telepresence, 2002.
- [35] T. Tanikawa, Y. Suzuki, K. Hirota, M. Hirose, Real world video avatar: Real-time and real-size transmission and presentation of human figure, in: Proc. of the Int. Conf. on Augmented Tele-existence, ACM, 2005, pp. 112–118. doi:10.1145/1152399.1152421.
- [36] G. Kurillo, R. Bajcsy, K. Nahrsted, O. Kreylos, Immersive 3d environment for remote collaboration and training of physical activities, in: IEEE Virtual Reality Conference, IEEE, 2008, pp. 269–270. doi:10.1109/vr.2008.4480795. 2
- [37] B. Petit, J.-D. Lesage, C. Menier, J. Allard, J.-S. Franco, B. Raffin, E. Boyer, F. Faure, Multicamera real-time 3d modeling for telepresence and remote collaboration, Int. Journal of Digital Multimedia Broadcasting 2010 (2010) 1–12. doi:10.1155/2010/247108. 2
- [38] C. Loop, C. Zhang, Z. Zhang, Real-time high-resolution sparse voxelization with application to image-based modeling, in: K. Fatahalian, C. Theobalt, J. Lehtinen (Eds.), Proc. of the High-Performance Graphics Conference, ACM, 2013, pp. 73–79. doi:10.1145/2492045.2492053. 2
- [39] S. Izadi, et al., Kinectfusion: Real-time 3d reconstruction and interaction using a moving depth camera, in: J. S. Pierce, M. Agrawal, S. R. Klemmer (Eds.), Proc. of the ACM Symp. on User Interface Software and Technology, ACM, 2011, pp. 559–568. doi:10.1145/2047196.2047270. 2
- [40] A. Maimone, H. Fuchs, Real-time volumetric 3d capture of room-sized scenes for telepresence, in: Proc. of the 3DTV-Conference, IEEE, 2012, pp. 1–4. doi:10.1109/3dtv.2012.6365430.
- [41] D. Molyneaux, S. Izadi, D. Kim, O. Hilliges, S. Hodges, X. Cao, A. Butler, H. Gellersen, Interactive environment-aware handheld projectors for pervasive computing spaces, in: J. Kay, P. Lukowicz, H. Tokuda, P. Olivier, A. Krüger (Eds.), Proc. of the Int. Conf. on Pervasive Computing, Vol. 7319, Springer Berlin Heidelberg, 2012, pp. 197–215. doi:10.1007/978-3-642-31205-2_13.
- [42] B. Jones, et al., Roomalive: Magical experiences enabled by scalable, adaptive projector-camera units, in: H. Benko, M. Dontcheva, D. Wigdor (Eds.), Proc. of the Annual Symp. on User Interface Software and Technology, ACM, 2014, pp. 637–644. doi:10.1145/2642918.2647383.
- [43] H. Fuchs, A. State, J. Bazin, Immersive 3d telepresence, Computer

- 47 (7) (2014) 46–52. doi:10.1109/mc.2014.185. 2
- [44] V. A. Nguyen, J. Lu, S. Zhao, D. T. Vu, H. Yang, D. L. Jones, M. N. Do, Item: Immersive telepresence for entertainment and meetings—a practical approach, *IEEE Journal of Selected Topics in Signal Processing* 9 (3) (2014) 546–561. doi:10.1109/jstsp.2014.2375819. 2
- [45] A. Jones, M. Lang, G. Fyffe, X. Yu, J. Busch, I. McDowall, M. Bolas, P. Debevec, Achieving eye contact in a one-to-many 3d video teleconferencing system, *ACM Transactions on Graphics (TOG)* 28 (3) (2009) 1–8. doi:10.1145/1576246.1531370.
- [46] J. Edelmann, P. Gerjets, P. Mock, A. Schilling, W. Strasser, Face2face—a system for multi-touch collaboration with telepresence, in: 2012 IEEE International Conference on Emerging Signal Processing Applications, IEEE, IEEE, 2012, pp. 159–162. doi:10.1109/espa.2012.6152470.
- [47] T. Pejša, J. Kantor, H. Benko, E. Ofek, A. Wilson, Room2room: Enabling life-size telepresence in a projected augmented reality environment, in: D. Gergle, M. R. Morris, P. Bjørn, J. A. Konstan (Eds.), Proceedings of the 19th ACM conference on computer-supported cooperative work & social computing, ACM, 2016, pp. 1716–1725. doi:10.1145/2818048.2819965.
- [48] T. Bell, S. Zhang, Holo reality: Real-time low-bandwidth 3d range video communications on consumer mobile devices with application to augmented reality, *Electronic Imaging* 2019 (16) (2019) 7–1. doi:10.2352/issn.2470-1173.2019.16.3dmp-007.
- [49] S. Cho, S.-w. Kim, J. Lee, J. Ahn, J. Han, Effects of volumetric capture avatars on social presence in immersive virtual environments, in: 2020 IEEE Conference on Virtual Reality and 3D User Interfaces (VR), IEEE, IEEE, 2020, pp. 26–34. doi:10.1109/vr46266.2020.00020. 2
- [50] S. Zhang, W. C. Ho, Tele-immersive interaction with intelligent virtual agents based on real-time 3d modeling, *Journal of Multimedia* 7 (1) (2012) 57. 2
- [51] R. S. Sodhi, B. R. Jones, D. Forsyth, B. P. Bailey, G. Maciocci, Bethere: 3d mobile collaboration with spatial input, in: W. E. Mackay, S. A. Brewster, S. Bødker (Eds.), Proceedings of the SIGCHI Conference on Human Factors in Computing Systems, CHI '13, Association for Computing Machinery, New York, NY, USA, 2013, p. 179–188. doi:10.1145/2470654.2470679.
- [52] X. Lu, J. Shen, S. Perugini, J. Yang, An immersive telepresence system using rgb-d sensors and head mounted display, in: 2015 IEEE International Symposium on Multimedia (ISM), IEEE, IEEE, 2015, pp. 453–458. doi:10.1109/ism.2015.108.
- [53] S. W. Greenwald, W. Corning, G. McDowell, P. Maes, J. Belcher, Electrovr: An electrostatic playground for collaborative, simulation-based exploratory learning in immersive virtual reality (2019).
- [54] T. Teo, L. Lawrence, G. A. Lee, M. Billingham, M. Adcock, Mixed reality remote collaboration combining 360 video and 3d reconstruction, in: S. A. Brewster, G. Fitzpatrick, A. L. Cox, V. Kostakos (Eds.), Proceedings of the 2019 CHI conference on human factors in computing systems, ACM, 2019, pp. 1–14. doi:10.1145/3290605.3300431.
- [55] F. E. Fadzli, A. W. Ismail, A robust real-time 3d reconstruction method for mixed reality telepresence, *International Journal of Innovative Computing* 10 (2) (11 2020). doi:10.11113/ijic.v10n2.265. 2
- [56] G. Bruder, F. Steinicke, A. Nüchter, Poster: Immersive point cloud virtual environments, in: A. Lécuyer, R. Lindeman, F. Steinicke (Eds.), 2014 IEEE Symposium on 3D User Interfaces (3DUI), IEEE, 2014, pp. 161–162. doi:10.1109/3dui.2014.6798870. 2
- [57] J. Young, T. Langlotz, S. Mills, H. Regenbrecht, Mobileportation: Nomadic telepresence for mobile devices, *Proceedings of the ACM on Interactive, Mobile, Wearable and Ubiquitous Technologies* 4 (2) (2020) 1–16. doi:10.1145/3397331. 2
- [58] D. Zingsheim, P. Stotko, S. Krumpfen, M. Weinmann, R. Klein, Collaborative vr-based 3d labeling of live-captured scenes by remote users, *IEEE Computer Graphics and Applications* 41 (4) (2021) 90–98. doi:10.1109/mcg.2021.3082267. 2
- [59] L. Peppoloni, F. Brizzi, C. A. Avizzano, E. Ruffaldi, Immersive ros-integrated framework for robot teleoperation, in: R. Lindeman, F. Steinicke, B. H. Thomas (Eds.), 2015 IEEE Symposium on 3D User Interfaces (3DUI), IEEE, IEEE, 2015, pp. 177–178. doi:10.1109/3dui.2015.7131758. 2
- [60] D. Krupke, S. Starke, L. Einig, J. Zhang, F. Steinicke, Prototyping of immersive hri scenarios, in: *Human-Centric Robotics: Proceedings of CLAWAR 2017: 20th International Conference on Climbing and Walking Robots and the Support Technologies for Mobile Machines*, World Scientific, WORLD SCIENTIFIC, 2018, pp. 537–544.
- [61] J. I. Lipton, A. J. Fay, D. Rus, Baxter’s homunculus: Virtual reality spaces for teleoperation in manufacturing, *IEEE Robotics and Automation Letters* 3 (1) (2017) 179–186. doi:10.1109/lra.2017.2737046.
- [62] M. Theofanidis, S. I. Sayed, A. Lioulemes, F. Makedon, Varm: Using virtual reality to program robotic manipulators, in: Proceedings of the 10th International Conference on Pervasive Technologies Related to Assistive Environments, ACM, 2017, pp. 215–221. doi:10.1145/3056540.3056541.
- [63] D. Whitney, E. Rosen, D. Ullman, E. Phillips, S. Tellex, Ros reality: A virtual reality framework using consumer-grade hardware for ros-enabled robots, in: 2018 IEEE/RSJ International Conference on Intelligent Robots and Systems (IROS), IEEE, IEEE, 2018, pp. 1–9. doi:10.1109/iros.2018.8593513.
- [64] E. Rosen, D. Whitney, M. Fishman, D. Ullman, S. Tellex, Mixed reality as a bidirectional communication interface for human-robot interaction, in: 2020 IEEE/RSJ International Conference on Intelligent Robots and Systems (IROS), IEEE, IEEE, 2020, pp. 11431–11438. doi:10.1109/iros45743.2020.9340822.
- [65] A. Naceri, D. Mazzanti, J. Bimbo, Y. T. Tefera, D. Prattichizzo, D. G. Caldwell, L. S. Mattos, N. Deshpande, The vicarios virtual reality interface for remote robotic teleoperation, *Journal of Intelligent & Robotic Systems* 101 (4) (2021) 1–16. doi:10.1007/s10846-021-01311-7. 2
- [66] P. Henry, M. Krainin, E. Herbst, X. Ren, D. Fox, Rgb-d mapping: Using depth cameras for dense 3d modeling of indoor environments, in: O. Khatib, V. Kumar, G. S. Sukhatme (Eds.), *Experimental robotics*, Vol. 79, Springer, Springer Berlin Heidelberg, 2014, pp. 477–491. doi:10.1007/978-3-642-28572-1_33. 3
- [67] R. A. Newcombe, S. Izadi, O. Hilliges, D. Molyneaux, D. Kim, A. J. Davison, P. Kohli, J. Shotton, S. Hodges, A. Fitzgibbon, Kinectfusion: Real-time dense surface mapping and tracking, in: 2011 10th IEEE International Symposium on Mixed and Augmented Reality, ISMAR 2011, IEEE, 2011, pp. 127–136. doi:10.1109/ismar.2011.6092378. 3, 6
- [68] S. Izadi, D. Kim, O. Hilliges, D. Molyneaux, R. Newcombe, P. Kohli, J. Shotton, S. Hodges, D. Freeman, A. Davison, et al., Kinectfusion: real-time 3d reconstruction and interaction using a moving depth camera, in: J. S. Pierce, M. Agrawala, S. R. Klemmer (Eds.), Proceedings of the 24th annual ACM symposium on User interface software and technology, ACM, 2011, pp. 559–568. doi:10.1145/2047196.2047270. 3
- [69] M. Nießner, M. Zollhöfer, S. Izadi, M. Stamminger, Real-time 3d reconstruction at scale using voxel hashing, *ACM Transactions on Graphics (ToG)* 32 (6) (2013) 1–11. doi:10.1145/2508363.2508374. 3, 6
- [70] O. Kähler, V. A. Prisacariu, C. Y. Ren, X. Sun, P. Torr, D. Murray, Very high frame rate volumetric integration of depth images on mobile devices, *IEEE transactions on visualization and computer graphics* 21 (11) (2015) 1241–1250. doi:10.1109/tvcg.2015.2459891.
- [71] O. Kähler, V. Prisacariu, J. Valentin, D. Murray, Hierarchical voxel block hashing for efficient integration of depth images, *IEEE Robotics and Automation Letters* 1 (1) (2015) 192–197. doi:10.1109/lra.2015.2512958.
- [72] O. Kähler, V. A. Prisacariu, D. W. Murray, Real-time large-scale dense 3d reconstruction with loop closure, in: B. Leibe, J. Matas, N. Sebe, M. Welling (Eds.), *European Conference on Computer Vision*, Vol. 9912, Springer, Springer International Publishing, 2016, pp. 500–516. doi:10.1007/978-3-319-46484-8_30.
- [73] V. A. Prisacariu, O. Kähler, S. Golodetz, M. Sapienza, T. Cavallari, P. H. Torr, D. W. Murray, Infinitam v3: A framework for large-scale 3d reconstruction with loop closure, *arXiv preprint arXiv:1708.00783 abs/1708.00783* (2017). 3
- [74] Y. Kuznetsov, J. Stuckler, B. Leibe, Semi-supervised deep learning for monocular depth map prediction, in: Proceedings of the IEEE conference on computer vision and pattern recognition, IEEE, 2017, pp. 6647–6655. doi:10.1109/cvpr.2017.238. 3
- [75] N. Yang, R. Wang, J. Stuckler, D. Cremers, Deep virtual stereo odometry: Leveraging deep depth prediction for monocular direct sparse odometry

- etry, in: V. Ferrari, M. Hebert, C. Sminchisescu, Y. Weiss (Eds.), Proceedings of the European Conference on Computer Vision (ECCV), Vol. 11212, Springer International Publishing, 2018, pp. 817–833. doi:10.1007/978-3-030-01237-3_50.
- [76] A. Kendall, Y. Gal, What uncertainties do we need in bayesian deep learning for computer vision?, *Advances in neural information processing systems* 30 (3 2017).
- [77] M. Klodt, A. Vedaldi, Supervising the new with the old: learning sfm from sfm, in: V. Ferrari, M. Hebert, C. Sminchisescu, Y. Weiss (Eds.), Proceedings of the European Conference on Computer Vision (ECCV), Vol. 11214, Springer International Publishing, 2018, pp. 698–713. doi:10.1007/978-3-030-01249-6_43.
- [78] N. Yang, L. v. Stumberg, R. Wang, D. Cremers, D3vo: Deep depth, deep pose and deep uncertainty for monocular visual odometry, in: Proceedings of the IEEE/CVF Conference on Computer Vision and Pattern Recognition, IEEE, 2020, pp. 1281–1292. doi:10.1109/cvpr42600.2020.00136.
- [79] J. Czarnowski, T. Laidlow, R. Clark, A. J. Davison, Deepfactors: Real-time probabilistic dense monocular slam, *IEEE Robotics and Automation Letters* 5 (2) (2020) 721–728. doi:10.1109/lra.2020.2965415.
- [80] F. Wimbauer, N. Yang, L. Von Stumberg, N. Zeller, D. Cremers, Monorec: Semi-supervised dense reconstruction in dynamic environments from a single moving camera, in: Proceedings of the IEEE/CVF Conference on Computer Vision and Pattern Recognition, IEEE, 2021, pp. 6112–6122. doi:10.1109/cvpr46437.2021.00605.3
- [81] C. Moore, T. Duckworth, R. Aspin, D. Roberts, Synchronization of images from multiple cameras to reconstruct a moving human, in: S. J. Turner, D. Roberts (Eds.), 2010 IEEE/ACM 14th International Symposium on Distributed Simulation and Real Time Applications, IEEE, IEEE, 2010, pp. 53–60. doi:10.1109/ds-rt.2010.15.3
- [82] D. S. Alexiadis, D. Zarpalas, P. Daras, Real-time, realistic full-body 3d reconstruction and texture mapping from multiple kinects, in: IVMS 2013, IEEE, IEEE, 2013, pp. 1–4. doi:10.1109/ivmspw.2013.6611939.
- [83] T. Duckworth, D. J. Roberts, Camera image synchronisation in multiple camera real-time 3d reconstruction of moving humans, in: D. J. Roberts, J. M. Pullen, G. K. Theodoropoulos, N. J. Avis (Eds.), 2011 IEEE/ACM 15th International Symposium on Distributed Simulation and Real Time Applications, IEEE, IEEE, 2011, pp. 138–144. doi:10.1109/ds-rt.2011.15.
- [84] D. Alexiadis, D. Zarpalas, P. Daras, Fast and smooth 3d reconstruction using multiple rgb-depth sensors, in: 2014 IEEE Visual Communications and Image Processing Conference, IEEE, IEEE, 2014, pp. 173–176. doi:10.1109/vcip.2014.7051532.
- [85] A. Islam, C. Scheel, A. S. Imran, O. Staadt, Fast and accurate 3d reproduction of a remote collaboration environment, in: R. Shumaker, S. J. Lackey (Eds.), International Conference on Virtual, Augmented and Mixed Reality, Vol. 8525, Springer, Springer International Publishing, 2014, pp. 351–362. doi:10.1007/978-3-319-07458-0_33.3
- [86] A. Tewari, O. Fried, J. Thies, V. Sitzmann, S. Lombardi, K. Sunkavalli, R. Martin-Brualla, T. Simon, J. Saragih, M. Nießner, et al., State of the art on neural rendering, in: *Computer Graphics Forum*, Vol. 39, Wiley Online Library, Wiley, 2020, pp. 701–727.3
- [87] A. Tewari, J. Thies, B. Mildenhall, P. Srinivasan, E. Tretschk, W. Yifan, C. Lassner, V. Sitzmann, R. Martin-Brualla, S. Lombardi, et al., Advances in neural rendering, in: *Computer Graphics Forum*, Vol. 41, Wiley Online Library, Wiley, 2022, pp. 703–735.3
- [88] B. Mildenhall, P. P. Srinivasan, M. Tancik, J. T. Barron, R. Ramamoorthi, R. Ng, Nerf: Representing scenes as neural radiance fields for view synthesis, *Communications of the ACM* 65 (1) (2021) 99–106. doi:10.1007/978-3-030-58452-8_24.3
- [89] C. Reiser, S. Peng, Y. Liao, A. Geiger, Kilonerf: Speeding up neural radiance fields with thousands of tiny mlps, in: Proceedings of the IEEE/CVF International Conference on Computer Vision, IEEE, 2021, pp. 14335–14345. doi:10.1109/iccv48922.2021.01407.3
- [90] S. Fridovich-Keil, A. Yu, M. Tancik, Q. Chen, B. Recht, A. Kanazawa, Plenoxels: Radiance fields without neural networks, in: Proceedings of the IEEE/CVF Conference on Computer Vision and Pattern Recognition, IEEE, 2022, pp. 5501–5510. doi:10.1109/cvpr52688.2022.00542.
- [91] Z. Chen, T. Funkhouser, P. Hedman, A. Tagliasacchi, Mobilenerf: Exploiting the polygon rasterization pipeline for efficient neural field rendering on mobile architectures, arXiv preprint arXiv:2208.00277 (7 2022).
- [92] K. Deng, A. Liu, J.-Y. Zhu, D. Ramanan, Depth-supervised nerf: Fewer views and faster training for free, in: Proceedings of the IEEE/CVF Conference on Computer Vision and Pattern Recognition, IEEE, 2022, pp. 12882–12891. doi:10.1109/cvpr52688.2022.01254.3
- [93] A. Chen, Z. Xu, A. Geiger, J. Yu, H. Su, Tensorf: Tensorial radiance fields, arXiv preprint arXiv:2203.09517 13692 (2022) 333–350. doi:10.1007/978-3-031-19824-3_20.
- [94] C. Sun, M. Sun, H.-T. Chen, Direct voxel grid optimization: Superfast convergence for radiance fields reconstruction, in: Proceedings of the IEEE/CVF Conference on Computer Vision and Pattern Recognition, IEEE, 2022, pp. 5459–5469. doi:10.1109/cvpr52688.2022.00538.
- [95] T. Müller, A. Evans, C. Schied, A. Keller, Instant neural graphics primitives with a multiresolution hash encoding, *ACM Trans. Graph.* 41 (4) (2022) 1–15. doi:10.1145/3528223.3530127.3
- [96] R. Martin-Brualla, N. Radwan, M. S. Sajjadi, J. T. Barron, A. Dosovitskiy, D. Duckworth, Nerf in the wild: Neural radiance fields for unconstrained photo collections, in: Proceedings of the IEEE/CVF Conference on Computer Vision and Pattern Recognition, IEEE, 2021, pp. 7210–7219. doi:10.1109/cvpr46437.2021.00713.3
- [97] X. Chen, Q. Zhang, X. Li, Y. Chen, Y. Feng, X. Wang, J. Wang, Hallucinated neural radiance fields in the wild, in: Proceedings of the IEEE/CVF Conference on Computer Vision and Pattern Recognition, IEEE, 2022, pp. 12943–12952. doi:10.1109/cvpr52688.2022.01260.3
- [98] K. Park, U. Sinha, J. T. Barron, S. Bouaziz, D. B. Goldman, S. M. Seitz, R. Martin-Brualla, Nerfies: Deformable neural radiance fields, in: Proceedings of the IEEE/CVF International Conference on Computer Vision, IEEE, 2021, pp. 5865–5874. doi:10.1109/iccv48922.2021.00581.3
- [99] A. Pumarola, E. Corona, G. Pons-Moll, F. Moreno-Noguer, D-nerf: Neural radiance fields for dynamic scenes, in: Proceedings of the IEEE/CVF Conference on Computer Vision and Pattern Recognition, IEEE, 2021, pp. 10318–10327. doi:10.1109/cvpr46437.2021.01018.
- [100] G. Gafni, J. Thies, M. Zollhofer, M. Nießner, Dynamic neural radiance fields for monocular 4d facial avatar reconstruction, in: Proceedings of the IEEE/CVF Conference on Computer Vision and Pattern Recognition, IEEE, 2021, pp. 8649–8658. doi:10.1109/cvpr46437.2021.00854.
- [101] E. Tretschk, A. Tewari, V. Golyanik, M. Zollhöfer, C. Lassner, C. Theobalt, Non-rigid neural radiance fields: Reconstruction and novel view synthesis of a dynamic scene from monocular video, in: Proceedings of the IEEE/CVF International Conference on Computer Vision, IEEE, 2021, pp. 12959–12970. doi:10.1109/iccv48922.2021.01272.
- [102] A. Raj, M. Zollhöfer, T. Simon, J. M. Saragih, S. Saito, J. Hays, S. Lombardi, Pixel-aligned volumetric avatars, in: IEEE Conference on Computer Vision and Pattern Recognition (CVPR), IEEE, 2021, pp. 11733–11742. doi:10.1109/cvpr46437.2021.01156.
- [103] A. Noguchi, X. Sun, S. Lin, T. Harada, Neural articulated radiance field, in: Proceedings of the IEEE/CVF International Conference on Computer Vision, IEEE, 2021, pp. 5762–5772. doi:10.1109/iccv48922.2021.00571.
- [104] W.-C. Tseng, H.-J. Liao, L. Yen-Chen, M. Sun, Cla-nerf: Category-level articulated neural radiance field, arXiv preprint arXiv:2202.00181 (5 2022). doi:10.1109/icra46639.2022.9812272.
- [105] S. Peng, J. Dong, Q. Wang, S. Zhang, Q. Shuai, X. Zhou, H. Bao, Animatable neural radiance fields for modeling dynamic human bodies, in: Proceedings of the IEEE/CVF International Conference on Computer Vision, IEEE, 2021, pp. 14314–14323. doi:10.1109/iccv48922.2021.01405.
- [106] K. Park, U. Sinha, P. Hedman, J. T. Barron, S. Bouaziz, D. B. Goldman, R. Martin-Brualla, S. M. Seitz, Hypernerf: A higher-dimensional representation for topologically varying neural radiance fields, arXiv preprint arXiv:2106.13228 (2021). doi:10.1145/3478513.3480487.
- [107] J. Chen, Y. Zhang, D. Kang, X. Zhe, L. Bao, X. Jia, H. Lu, Animat-

- able neural radiance fields from monocular rgb videos, arXiv preprint arXiv:2106.13629 (6 2021).
- [108] L. Liu, M. Habermann, V. Rudnev, K. Sarkar, J. Gu, C. Theobalt, Neural actor: Neural free-view synthesis of human actors with pose control, *ACM Transactions on Graphics (TOG)* 40 (6) (2021) 1–16. doi:10.1145/3478513.3480528. 3
- [109] Z. Li, S. Niklaus, N. Snavely, O. Wang, Neural scene flow fields for space-time view synthesis of dynamic scenes, in: *Proceedings of the IEEE/CVF Conference on Computer Vision and Pattern Recognition*, IEEE, 2021, pp. 6498–6508. doi:10.1109/cvpr46437.2021.00643. 3
- [110] W. Xian, J.-B. Huang, J. Kopf, C. Kim, Space-time neural irradiance fields for free-viewpoint video, in: *Proceedings of the IEEE/CVF Conference on Computer Vision and Pattern Recognition*, IEEE, 2021, pp. 9421–9431. doi:10.1109/cvpr46437.2021.00930.
- [111] Y. Du, Y. Zhang, H.-X. Yu, J. B. Tenenbaum, J. Wu, Neural radiance flow for 4d view synthesis and video processing, in: *2021 IEEE/CVF International Conference on Computer Vision (ICCV)*, IEEE Computer Society, IEEE, 2021, pp. 14304–14314. doi:10.1109/iccv48922.2021.01406.
- [112] S. Peng, Y. Zhang, Y. Xu, Q. Wang, Q. Shuai, H. Bao, X. Zhou, Neural body: Implicit neural representations with structured latent codes for novel view synthesis of dynamic humans, in: *Proceedings of the IEEE/CVF Conference on Computer Vision and Pattern Recognition*, IEEE, 2021, pp. 9054–9063. doi:10.1109/cvpr46437.2021.00894.
- [113] C. Gao, A. Saraf, J. Kopf, J.-B. Huang, Dynamic view synthesis from dynamic monocular video, in: *Proceedings of the IEEE/CVF International Conference on Computer Vision*, IEEE, 2021, pp. 5712–5721. doi:10.1109/iccv48922.2021.00566.
- [114] T. Li, M. Slavcheva, M. Zollhoefer, S. Green, C. Lassner, C. Kim, T. Schmidt, S. Lovegrove, M. Goesele, R. Newcombe, et al., Neural 3d video synthesis from multi-view video, in: *Proceedings of the IEEE/CVF Conference on Computer Vision and Pattern Recognition*, IEEE, 2022, pp. 5521–5531. doi:10.1109/cvpr52688.2022.00544. 3
- [115] L. Yen-Chen, P. Florence, J. T. Barron, A. Rodriguez, P. Isola, T.-Y. Lin, inerf: Inverting neural radiance fields for pose estimation, in: *2021 IEEE/RSJ International Conference on Intelligent Robots and Systems (IROS)*, IEEE, IEEE, 2021, pp. 1323–1330. doi:10.1109/iros51168.2021.9636708. 3
- [116] S.-Y. Su, F. Yu, M. Zollhoefer, H. Rhodin, A-nerf: Surface-free human 3d pose refinement via neural rendering, arXiv preprint arXiv:2102.06199 (2021).
- [117] Z. Wang, S. Wu, W. Xie, M. Chen, V. A. Prisacariu, Nerf-: Neural radiance fields without known camera parameters, arXiv preprint arXiv:2102.07064 (2 2021).
- [118] E. Sucar, S. Liu, J. Ortiz, A. J. Davison, imap: Implicit mapping and positioning in real-time, in: *Proceedings of the IEEE/CVF International Conference on Computer Vision*, IEEE, 2021, pp. 6229–6238. doi:10.1109/iccv48922.2021.00617. 3
- [119] Z. Zhu, S. Peng, V. Larsson, W. Xu, H. Bao, Z. Cui, M. R. Oswald, M. Pollefeys, Nice-slam: Neural implicit scalable encoding for slam, in: *Proceedings of the IEEE/CVF Conference on Computer Vision and Pattern Recognition*, IEEE, 2022, pp. 12786–12796. doi:10.1109/cvpr52688.2022.01245. 3
- [120] Q. Meng, A. Chen, H. Luo, M. Wu, H. Su, L. Xu, X. He, J. Yu, Gnerf: Gan-based neural radiance field without posed camera, in: *Proceedings of the IEEE/CVF International Conference on Computer Vision*, IEEE, 2021, pp. 6351–6361. doi:10.1109/iccv48922.2021.00629.
- [121] C.-H. Lin, W.-C. Ma, A. Torralba, S. Lucey, Barf: Bundle-adjusting neural radiance fields, in: *Proceedings of the IEEE/CVF International Conference on Computer Vision*, IEEE, 2021, pp. 5741–5751. doi:10.1109/iccv48922.2021.00569.
- [122] Y. Jeong, S. Ahn, C. Choy, A. Anandkumar, M. Cho, J. Park, Self-calibrating neural radiance fields, in: *Proceedings of the IEEE/CVF International Conference on Computer Vision*, IEEE, 2021, pp. 5846–5854. doi:10.1109/iccv48922.2021.00579. 3
- [123] S. Vora, N. Radwan, K. Greff, H. Meyer, K. Genova, M. S. Sajjadi, E. Pot, A. Tagliasacchi, D. Duckworth, Nesf: Neural semantic fields for generalizable semantic segmentation of 3d scenes, arXiv preprint arXiv:2111.13260 abs/2111.13260 (11 2021). 3
- [124] S. Zhi, T. Laidlaw, S. Leutenegger, A. J. Davison, In-place scene labelling and understanding with implicit scene representation, in: *Proceedings of the IEEE/CVF International Conference on Computer Vision*, IEEE, 2021, pp. 15838–15847. doi:10.1109/iccv48922.2021.01554.
- [125] X. Fu, S. Zhang, T. Chen, Y. Lu, L. Zhu, X. Zhou, A. Geiger, Y. Liao, Panoptic nerf: 3d-to-2d label transfer for panoptic urban scene segmentation, arXiv preprint arXiv:2203.15224 (9 2022). doi:10.1109/3dv57658.2022.00042. 3
- [126] Y. Wei, S. Liu, Y. Rao, W. Zhao, J. Lu, J. Zhou, Nerfingmvs: Guided optimization of neural radiance fields for indoor multi-view stereo, in: *Proceedings of the IEEE/CVF International Conference on Computer Vision*, IEEE, 2021, pp. 5610–5619. doi:10.1109/iccv48922.2021.00556. 3
- [127] B. Roessle, J. T. Barron, B. Mildenhall, P. P. Srinivasan, M. Nießner, Dense depth priors for neural radiance fields from sparse input views, in: *Proceedings of the IEEE/CVF Conference on Computer Vision and Pattern Recognition*, IEEE, 2022, pp. 12892–12901. doi:10.1109/cvpr52688.2022.01255.
- [128] K. Rematas, A. Liu, P. P. Srinivasan, J. T. Barron, A. Tagliasacchi, T. Funkhouser, V. Ferrari, Urban radiance fields, in: *Proceedings of the IEEE/CVF Conference on Computer Vision and Pattern Recognition*, IEEE, 2022, pp. 12932–12942. doi:10.1109/cvpr52688.2022.01259.
- [129] B. Attal, E. Laidlaw, A. Gokaslan, C. Kim, C. Richardt, J. Tompkin, M. O’Toole, Törf: Time-of-flight radiance fields for dynamic scene view synthesis, *Advances in neural information processing systems* 34 (2021) 26289–26301. 3
- [130] M. Tancik, V. Casser, X. Yan, S. Pradhan, B. Mildenhall, P. P. Srinivasan, J. T. Barron, H. Kretzschmar, Block-nerf: Scalable large scene neural view synthesis, in: *Proceedings of the IEEE/CVF Conference on Computer Vision and Pattern Recognition*, IEEE, 2022, pp. 8248–8258. doi:10.1109/cvpr52688.2022.00807. 3
- [131] H. Turki, D. Ramanan, M. Satyanarayanan, Mega-nerf: Scalable construction of large-scale nerfs for virtual fly-throughs, in: *Proceedings of the IEEE/CVF Conference on Computer Vision and Pattern Recognition*, IEEE, 2022, pp. 12922–12931. doi:10.1109/cvpr52688.2022.01258. 3
- [132] J. Cho, S. Nam, D. Rho, J. H. Ko, E. Park, Streamable neural fields, in: S. Avidan, G. J. Brostow, M. Cissé, G. M. Farinella, T. Hassner (Eds.), *European Conference on Computer Vision*, Vol. 13680, Springer, Springer Nature Switzerland, 2022, pp. 595–612. doi:10.1007/978-3-031-20044-1_34. 3
- [133] Z. Zhu, S. Peng, V. Larsson, Z. Cui, M. R. Oswald, A. Geiger, M. Pollefeys, Nicer-slam: Neural implicit scene encoding for rgb slam, arXiv preprint arXiv:2302.03594 (2023). 3
- [134] A. Rosinol, J. J. Leonard, L. Carlone, Nerf-slam: Real-time dense monocular slam with neural radiance fields, arXiv preprint arXiv:2210.13641 (2022). 3
- [135] X. Zhang, S. Bi, K. Sunkavalli, H. Su, Z. Xu, Nerfusion: Fusing radiance fields for large-scale scene reconstruction, in: *Proceedings of the IEEE/CVF Conference on Computer Vision and Pattern Recognition*, 2022, pp. 5449–5458. 3
- [136] D.-H. Kim, J.-H. Kim, Effective background model-based rgb-d dense visual odometry in a dynamic environment, *IEEE Transactions on Robotics* 32 (6) (2016) 1565–1573. doi:10.1109/tro.2016.2609395. 3
- [137] R. Scona, M. Jaimez, Y. R. Petillot, M. Fallon, D. Cremers, Static-fusion: Background reconstruction for dense rgb-d slam in dynamic environments, in: *2018 IEEE International Conference on Robotics and Automation (ICRA)*, IEEE, IEEE, 2018, pp. 3849–3856. doi:10.1109/icra.2018.8460681.
- [138] Y. Fan, H. Han, Y. Tang, T. Zhi, Dynamic objects elimination in slam based on image fusion, *Pattern Recognition Letters* 127 (2019) 191–201. doi:10.1016/j.patrec.2018.10.024.
- [139] B. Bescos, J. M. Fácil, J. Civera, J. Neira, Dynaslam: Tracking, mapping, and inpainting in dynamic scenes, *IEEE Robotics and Automation Letters* 3 (4) (2018) 4076–4083. doi:10.1109/lra.2018.2860039.
- [140] C. Yu, Z. Liu, X.-J. Liu, F. Xie, Y. Yang, Q. Wei, Q. Fei, Ds-slam: A semantic visual slam towards dynamic environments, in: *2018*

- IEEE/RSJ International Conference on Intelligent Robots and Systems (IROS), IEEE, IEEE, 2018, pp. 1168–1174. doi:10.1109/iros.2018.8593691.
- [141] T. Zhang, H. Zhang, Y. Li, Y. Nakamura, L. Zhang, Flowfusion: Dynamic dense rgb-d slam based on optical flow, in: 2020 IEEE International Conference on Robotics and Automation (ICRA), IEEE, IEEE, 2020, pp. 7322–7328. doi:10.1109/icra40945.2020.9197349.
- [142] B. Xu, W. Li, D. Tzoumanikas, M. Bloesch, A. Davison, S. Leutenegger, Mid-fusion: Octree-based object-level multi-instance dynamic slam, in: 2019 International Conference on Robotics and Automation (ICRA), IEEE, IEEE, 2019, pp. 5231–5237. doi:10.1109/icra.2019.8794371. 3
- [143] J. Stückler, S. Behnke, Efficient dense rigid-body motion segmentation and estimation in rgb-d video, International Journal of Computer Vision 113 (3) (2015) 233–245. doi:10.1007/s11263-014-0796-3. 3
- [144] J. Wulff, L. Sevilla-Lara, M. J. Black, Optical flow in mostly rigid scenes, in: Proceedings of the IEEE Conference on Computer Vision and Pattern Recognition, IEEE, 2017, pp. 4671–4680. doi:10.1109/cvpr.2017.731.
- [145] S. Li, D. Lee, Rgb-d slam in dynamic environments using static point weighting, IEEE Robotics and Automation Letters 2 (4) (2017) 2263–2270. doi:10.1109/lra.2017.7274759.
- [146] M. Rünz, L. Agapito, Co-fusion: Real-time segmentation, tracking and fusion of multiple objects, in: 2017 IEEE International Conference on Robotics and Automation (ICRA), IEEE, IEEE, 2017, pp. 4471–4478. doi:10.1109/icra.2017.7989518.
- [147] M. Runz, M. Buffier, L. Agapito, Maskfusion: Real-time recognition, tracking and reconstruction of multiple moving objects, in: D. Chu, J. L. Gabbard, J. Grubert, H. Regenbrecht (Eds.), 2018 IEEE International Symposium on Mixed and Augmented Reality (ISMAR), IEEE, IEEE, 2018, pp. 10–20. doi:10.1109/ismar.2018.00024.
- [148] M. Henein, J. Zhang, R. Mahony, V. Ila, Dynamic slam: The need for speed, in: 2020 IEEE International Conference on Robotics and Automation (ICRA), IEEE, 2020, pp. 2123–2129. doi:10.1109/icra40945.2020.9196895. 3
- [149] H. Li, L. Luo, D. Vlasic, P. Peers, J. Popović, M. Pauly, S. Rusinkiewicz, Temporally coherent completion of dynamic shapes, ACM Transactions on Graphics (TOG) 31 (1) (2012) 1–11. doi:10.1145/2077341.2077343. 3
- [150] M. Keller, D. Lefloch, M. Lambers, S. Izadi, T. Weyrich, A. Kolb, Real-time 3d reconstruction in dynamic scenes using point-based fusion, in: 2013 International Conference on 3D Vision-3DV 2013, IEEE, IEEE, 2013, pp. 1–8. doi:10.1109/3dv.2013.9.
- [151] M. Ye, R. Yang, Real-time simultaneous pose and shape estimation for articulated objects using a single depth camera, in: Proceedings of the IEEE Conference on Computer Vision and Pattern Recognition, IEEE, 2014, pp. 2345–2352. doi:10.1109/cvpr.2014.301.
- [152] R. A. Newcombe, D. Fox, S. M. Seitz, Dynamicfusion: Reconstruction and tracking of non-rigid scenes in real-time, in: Proceedings of the IEEE conference on computer vision and pattern recognition, IEEE, 2015, pp. 343–352. doi:10.1109/cvpr.2015.7298631.
- [153] K. Guo, F. Xu, Y. Wang, Y. Liu, Q. Dai, Robust non-rigid motion tracking and surface reconstruction using l0 regularization, in: Proceedings of the IEEE International Conference on Computer Vision, IEEE, 2015, pp. 3083–3091. doi:10.1109/iccv.2015.353.
- [154] T. Whelan, R. F. Salas-Moreno, B. Glocker, A. J. Davison, S. Leutenegger, Elasticfusion: Real-time dense slam and light source estimation, The International Journal of Robotics Research 35 (14) (2016) 1697–1716. 3
- [155] M. Innmann, M. Zollhöfer, M. Nießner, C. Theobalt, M. Stamminger, Volumedeform: Real-time volumetric non-rigid reconstruction, in: B. Leibe, J. Matas, N. Sebe, M. Welling (Eds.), European conference on computer vision, Vol. 9912, Springer, Springer International Publishing, 2016, pp. 362–379. doi:10.1007/978-3-319-46484-8_22.
- [156] M. Dou, S. Khamis, Y. Degtyarev, P. Davidson, S. R. Fanello, A. Kowdle, S. O. Escolano, C. Rhemann, D. Kim, J. Taylor, et al., Fusion4d: Real-time performance capture of challenging scenes, ACM Transactions on Graphics (ToG) 35 (4) (2016) 1–13.
- [157] H. Zhang, F. Xu, Mixedfusion: Real-time reconstruction of an indoor scene with dynamic objects, IEEE transactions on visualization and computer graphics 24 (12) (2017) 3137–3146. doi:10.1109/tvcg.2017.2786233.
- [158] M. Slavcheva, M. Baust, D. Cremers, S. Ilic, Killingfusion: Non-rigid 3d reconstruction without correspondences, in: Proceedings of the IEEE Conference on Computer Vision and Pattern Recognition, IEEE, 2017, pp. 1386–1395. doi:10.1109/cvpr.2017.581.
- [159] M. Jaimez, C. Kerl, J. Gonzalez-Jimenez, D. Cremers, Fast odometry and scene flow from rgb-d cameras based on geometric clustering, in: 2017 IEEE International Conference on Robotics and Automation (ICRA), IEEE, IEEE, 2017, pp. 3992–3999. doi:10.1109/icra.2017.7989459.
- [160] M. Slavcheva, M. Baust, S. Ilic, Sobolevfusion: 3d reconstruction of scenes undergoing free non-rigid motion, in: Proceedings of the IEEE conference on computer vision and pattern recognition, IEEE, 2018, pp. 2646–2655. doi:10.1109/cvpr.2018.00280.
- [161] M. Strecke, J. Stückler, Em-fusion: Dynamic object-level slam with probabilistic data association, in: Proceedings of the IEEE/CVF International Conference on Computer Vision, IEEE, 2019, pp. 5865–5874. doi:10.1109/iccv.2019.00596. 3
- [162] G. Jocher, A. Chaurasia, J. Qiu, Yolov8: The state-of-the-art yolo model, <https://github.com/ultralytics/ultralytics>, accessed: 2023-02-21 (2023). 3, 4, 9
- [163] Nvidia Corporation, Nvidia optical flow sdk, <https://developer.nvidia.com/opticalflow-sdk>, accessed: 2023-02-21 (2019). 4, 9
- [164] Q.-Y. Zhou, J. Park, V. Koltun, Open3d: A modern library for 3d data processing, arXiv:1801.09847 (1 2018). 4
- [165] Y. Collet, C. Turner, Smaller and faster data compression with zstandard, <https://engineering.fb.com/2016/08/31/core-data/smaller-and-faster-data-compression-with-zstandard/>, accessed: 2023-02-08 (2016). 6
- [166] K. Han, R. S. Rezende, B. Ham, K.-Y. K. Wong, M. Cho, C. Schmid, J. Ponce, Snet: Learning semantic correspondence, in: Proceedings of the IEEE international conference on computer vision, IEEE, 2017, pp. 1831–1840. doi:10.1109/iccv.2017.203. 9
- [167] A. Kirillov, Y. Wu, K. He, R. Girshick, Pointrend: Image segmentation as rendering, in: Proceedings of the IEEE/CVF conference on computer vision and pattern recognition, IEEE, 2020, pp. 9799–9808. doi:10.1109/cvpr42600.2020.00982. 9
- [168] K. He, G. Gkioxari, P. Dollár, R. Girshick, Mask r-cnn, in: Proceedings of the IEEE international conference on computer vision, Vol. 42, Institute of Electrical and Electronics Engineers (IEEE), 2017, pp. 2961–2969. doi:10.1109/tpami.2018.2844175. 9
- [169] X. Wang, R. Zhang, T. Kong, L. Li, C. Shen, Solov2: Dynamic and fast instance segmentation, Proc. Advances in Neural Information Processing Systems (NeurIPS) (3 2020). 9
- [170] S. Jiang, D. Campbell, Y. Lu, H. Li, R. Hartley, Learning to estimate hidden motions with global motion aggregation, in: Proceedings of the IEEE/CVF International Conference on Computer Vision, IEEE, 2021, pp. 9772–9781. doi:10.1109/iccv48922.2021.00963. 9
- [171] Z. Teed, J. Deng, Raft: Recurrent all-pairs field transforms for optical flow, in: A. Vedaldi, H. Bischof, T. Brox, J.-M. Frahm (Eds.), European conference on computer vision, Vol. 12347, Springer, Springer International Publishing, 2020, pp. 402–419. doi:10.1007/978-3-030-58536-5_24. 9
- [172] S. Zhao, Y. Sheng, Y. Dong, E. I. Chang, Y. Xu, et al., Maskflownet: Asymmetric feature matching with learnable occlusion mask, in: Proceedings of the IEEE/CVF Conference on Computer Vision and Pattern Recognition, IEEE, 2020, pp. 6278–6287. doi:10.1109/cvpr42600.2020.00631. 9
- [173] T.-W. Hui, X. Tang, C. C. Loy, A lightweight optical flow cnn—revisiting data fidelity and regularization, IEEE transactions on pattern analysis and machine intelligence 43 (8) (2020) 2555–2569. doi:10.1109/tpami.2020.2976928. 9